JOURNAL OF PETROLOGY | VOLUME 52 | NUMBER 6 | PAGES 1107–1141 | 2011 | doi:10.1093/petrology/egr020

Enriched Basaltic Andesites from Mid-crustal Fractional Crystallization, Recharge, and Assimilation (Pilavo Volcano, Western Cordillera of Ecuador)

MASSIMO CHIARADIA[1], OTHMAR MÜNTENER[2] AND BERNARDO BEATE[3]

[1]SECTION OF EARTH AND ENVIRONMENTAL SCIENCES, DEPARTMENT OF MINERALOGY, UNIVERSITY OF GENEVA, RUE DES MARAÎCHERS 13, 1205 GENEVA, SWITZERLAND

[2]INSTITUTE OF MINERALOGY AND GEOCHEMISTRY, UNIVERSITY OF LAUSANNE, ANTHROPOLE, CH-1015 LAUSANNE, SWITZERLAND

[3]DEPARTMENT OF GEOLOGY, ESCUELA POLITECNICA NACIÓNAL, QUITO, ECUADOR

RECEIVED OCTOBER 19, 2010; ACCEPTED APRIL 19, 2011
ADVANCE ACCESS PUBLICATION JUNE 8, 2011

The origin of andesite is an important issue in petrology because andesite is the main eruptive product at convergent margins, corresponds to the average crustal composition and is often associated with major Cu–Au mineralization. In this study we present petrographic, mineralogical, geochemical and isotopic data for basaltic andesites of the latest Pleistocene Pilavo volcano, one of the most frontal volcanoes of the Ecuadorian Quaternary arc, situated upon thick (30–50 km) mafic crust composed of accreted Cretaceous oceanic plateau rocks and overlying mafic to intermediate Late Cretaceous–Late Tertiary magmatic arcs. The Pilavo rocks are basaltic andesites (54–57·5 wt % SiO_2) with a tholeiitic affinity as opposed to the typical calc-alkaline high-silica andesites and dacites (SiO_2 59–66 wt %) of other frontal arc volcanoes of Ecuador (e.g. Pichincha, Pululahua). They have much higher incompatible element contents (e.g. Sr 650–1350 ppm, Ba 650–1800 ppm, Zr 100–225 ppm, Th 5–25 ppm, La 15–65 ppm) and Th/La ratios (0·28–0·36) than Pichincha and Pululahua, and more primitive Sr ($^{87}Sr/^{86}Sr$ ~0·7038–0·7039) and Nd (ε_{Nd} ~ +5·5 to +6·1) isotopic signatures. Pilavo andesites have geochemical affinities with modern and recent high-MgO andesites (e.g. low-silica adakites, Setouchi sanukites) and, especially, with Archean sanukitoids, for both of which incompatible element enrichments are believed to result from interactions of slab melts with peridotitic mantle. Petrographic, mineral chemistry, bulk-rock geochemical and isotopic data indicate that the Pilavo magmatic rocks have evolved through three main stages: (1) generation of a basaltic magma in the mantle wedge region by flux melting induced by slab-derived fluids (aqueous, supercritical or melts); (2) high-pressure differentiation of the basaltic melt (at the mantle–crust boundary or at lower crustal levels) through sustained fractionation of olivine and clinopyroxene, leading to hydrous, high-alumina basaltic andesite melts with a tholeiitic affinity, enriched in incompatible elements and strongly impoverished in Ni and Cr; (3) establishment of one or more mid-crustal magma storage reservoirs in which the magmas evolved through dominant amphibole and clinopyroxene (but no plagioclase) fractionation accompanied by assimilation of the modified plutonic roots of the arc and recharge by incoming batches of more primitive magma from depth. The latter process has resulted in strongly increasing incompatible element concentrations in the Pilavo basaltic andesites, coupled with slightly increasing crustal isotopic signatures and a shift towards a more calc-alkaline affinity. Our data show that, although ultimately originating from the slab, incompatible element abundances in arc andesites with primitive isotopic signatures can be significantly enhanced by intra-crustal processes within a thick juvenile mafic crust, thus providing an additional process for the generation of enriched andesites.

*Corresponding author. Telephone: +41 22 379 66 34. Fax: +41 22 379 32 10. E-mail: Massimo.Chiaradia@unige.ch

KEY WORDS: *andesite; assimilation; fractional crystallization; recharge; Ecuador*

INTRODUCTION

Establishing the origin of andesitic rocks is an important goal of petrology because andesite is the main eruptive product at convergent margins, it corresponds to the average crustal composition (e.g. Gill, 1981; Rudnick & Gao, 2004) and it is closely associated with major porphyry-related Cu–Au mineralization (e.g. Richards, 2003). Various petrogenetic models have been proposed for the genesis of andesite, including, among others, partial melting of peridotite under hydrous conditions (e.g. Kushiro, 1969; Hirose, 1997; Wood & Turner, 2009), partial melting of the subducting oceanic crust (e.g. Taylor *et al.*, 1969), crystal fractionation of mantle-derived basalts (e.g. Crawford *et al.*, 1987; Müntener *et al.*, 2001; Grove *et al.*, 2003), mixing between mantle-derived basalt and crust-derived felsic melts (e.g. Tatsumi & Kogiso, 2003) or assimilation of the plutonic roots of arcs (Reubi & Blundy, 2008). In all these models, the geochemical characteristics of arc andesites imply a contribution from the subducted slab (sediments and oceanic crust) in the form of aqueous fluids, supercritical liquids or hydrous silicate melts acting as the metasomatic agent responsible for the flux melting of the mantle wedge, with supercritical fluids and hydrous silicate melts being the most likely fluxing agents (e.g. Kessel *et al.*, 2005; Hermann *et al.*, 2006). In particular, high-MgO andesites [or low-silica adakites of Martin *et al.* (2005)] with high concentrations of large ion lithophile elements (LILE) and light rare earth elements (LREE), high Sr/Y and La/Yb, and heavy REE (HREE) depletion, like those of the Miocene Setouchi belt of Japan and of the western part of the Aleutian arc, are considered to derive from melting of peridotite previously metasomatized by slab melts or from the incomplete reaction of slab melts with the peridotitic mantle wedge (Rapp *et al.*, 1999; Kelemen *et al.*, 2003; Martin *et al.*, 2005; Tatsumi, 2006). Because such rocks are similar to the average crustal composition and bear strong similarities to Archean sanukitoids (Shirey & Hanson, 1984), their petrogenesis is important for the understanding of continental crust formation processes (e.g. Tatsumi, 2006; Rapp *et al.*, 2010).

In the present study we investigate andesitic rocks from Pilavo volcano, one of the most frontal volcanoes of the Ecuadorian Quaternary arc. The petrogenesis of these rocks is of particular interest because Pilavo lavas are incompatible element-rich basaltic andesites to low-SiO_2 andesites with a tholeiitic affinity as opposed to the typical calc-alkaline high-SiO_2 andesites and dacites of the other frontal arc volcanoes of Ecuador (e.g. Pichincha, Pululahua). Like all frontal arc volcanoes of the Western Cordillera of Ecuador (e.g. Feininger & Seguin, 1983), Pilavo sits above Cretaceous mafic oceanic crust, excluding the possibility that its incompatible element enrichment is acquired from assimilation of mature continental crust. The enriched geochemistry of Pilavo rocks resembles that of modern low-silica adakites (e.g. Setouchi sanukite) and, especially, that of Archean sanukitoids, from which Pilavo differs, none the less, in having variably lower MgO and significantly lower Ni and Cr contents. Investigation of the Pilavo basaltic andesites thus has the potential to shed further light on the origin of enriched andesitic rocks and their significance with respect to continental crust formation processes, as well as on the coupled occurrence of tholeiitic and calc-alkaline rocks within the same arc and volcanic edifice (e.g. Hora *et al.*, 2009).

GEODYNAMIC SETTING AND ARC MAGMATISM

Present-day arc volcanism in the Ecuadorian Andes is the result of subduction of the 12–20 Myr old Nazca plate and overlying aseismic Carnegie Ridge (Fig. 1). The active to recent volcanic arc of Ecuador extends over more than 100 km across the Andean chain (Fig. 1) starting in the Western Cordillera, passing through the Interandean Valley and the Eastern Cordillera, and ending in the Andean foreland (Oriente) where both alkaline (Sumaco, Pan de Azucar, Puyo) and calc-alkaline (Reventador) volcanoes occur. Such a broad volcanic arc (>100 km) contrasts with the narrower volcanic arc immediately to the north in Colombia, and with the volcanic gap south of 2°S owing to the Peruvian flat slab segment (Barazangi & Isacks, 1976). The subduction of the aseismic Carnegie Ridge in coincidence with the Ecuadorian volcanic arc suggests a direct link with such a broad arc. It has been proposed that subduction of the Carnegie Ridge beneath the continental crust of Ecuador has caused an increased coupling between the subducting and overriding plates (e.g. Ego *et al.*, 1996; Gutscher *et al.*, 1999; Graindorge *et al.*, 2004). Gutscher *et al.* (1999) suggested that flat subduction was related to the subduction of the Carnegie Ridge flanked by subduction of two steeper segments north and south of the Carnegie Ridge. In contrast, Guillier *et al.* (2001) concluded that subduction of the Carnegie Ridge segment is not flat, but regularly dipping at an angle of 25° (see also Lonsdale, 1978; Pennington, 1981; Prévot *et al.*, 1996) although immediately to the north of it the dip increases slightly to 30°.

The estimated crustal thickness beneath the Western Cordillera, where Pilavo is situated, ranges between 25–30 km (Feininger & Seguin, 1983) and 40–50 km (Guillier *et al.*, 2001). Gravimetric (Feininger & Seguin, 1983) and isotopic (Chiaradia & Fontboté, 2001; Chiaradia, 2009) data indicate the presence of mafic crust beneath the Western Cordillera of Ecuador (Fig. 1), with oceanic plateau-like geochemical characteristics (e.g. Kerr

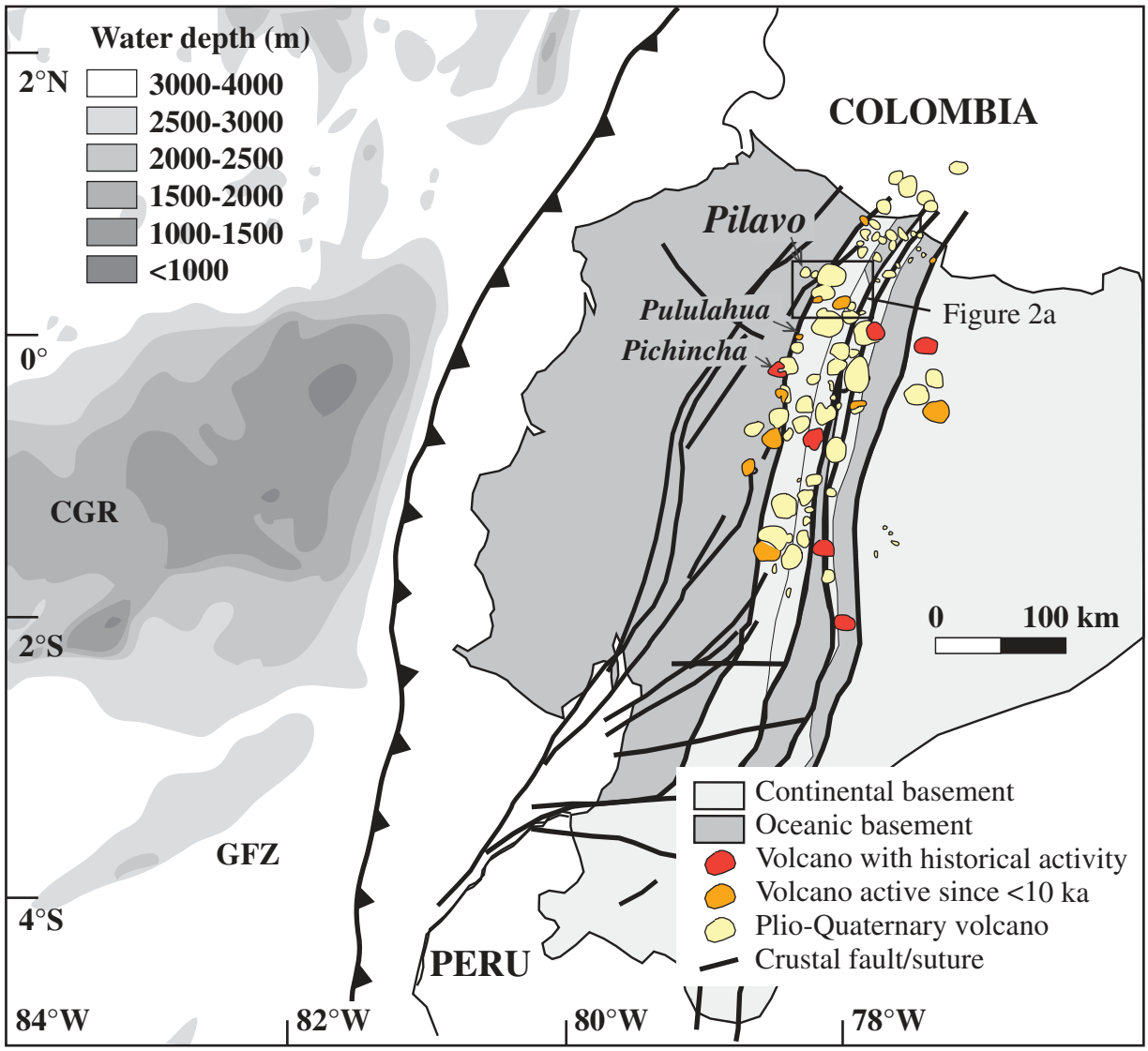

Fig. 1. Map of Ecuador showing the main topographic features of the subducting plates (CGR, Carnegie Ridge; GFZ, Grijalva Fracture Zone) and the localization of recent and active volcanoes in Ecuador (modified after Litherland *et al.*, 1994; Corredor, 2003).

et al., 2002; Mamberti *et al.*, 2003). The oceanic plateau crust represents an exotic terrane (e.g. Feininger, 1987; Jaillard *et al.*, 1990, 1997; Spikings *et al.*, 2005), derived from the large Caribbean–Colombian Oceanic Plateau (CCOP), which was accreted to the continental margin of Ecuador during Late Cretaceous times (Vallejo *et al.*, 2006, 2009).

Various studies have highlighted systematic compositional changes in the lavas of the Ecuadorian arc from the frontal to the back-arc region (e.g. Barragan *et al.*, 1998; Bourdon *et al.*, 2003; Bryant *et al.*, 2006; Chiaradia *et al.*, 2009). These variations have been interpreted as the result of progressively smaller degrees of partial melting of the mantle wedge metasomatized by decreasing amounts of slab fluids or melts towards the back-arc (the K–h relationship: Dickinson, 1975).

LOCAL GEOLOGY

Pilavo volcano (0°31′N, 78°22′W) is located about 20 km trenchward of the main axis of the active volcanic front (Figs 1 and 2a), which follows the crest of the Western Cordillera of the Ecuadorian Andes. It is thus one of the closest volcanoes to the trench of the Northern Andes subduction system, located about 230 km to the west of Pilavo (Fig. 1). The deep basement of Pilavo, like that of several other frontal volcanoes of the Western Cordillera of Ecuador, consists of oceanic plateau mafic crust

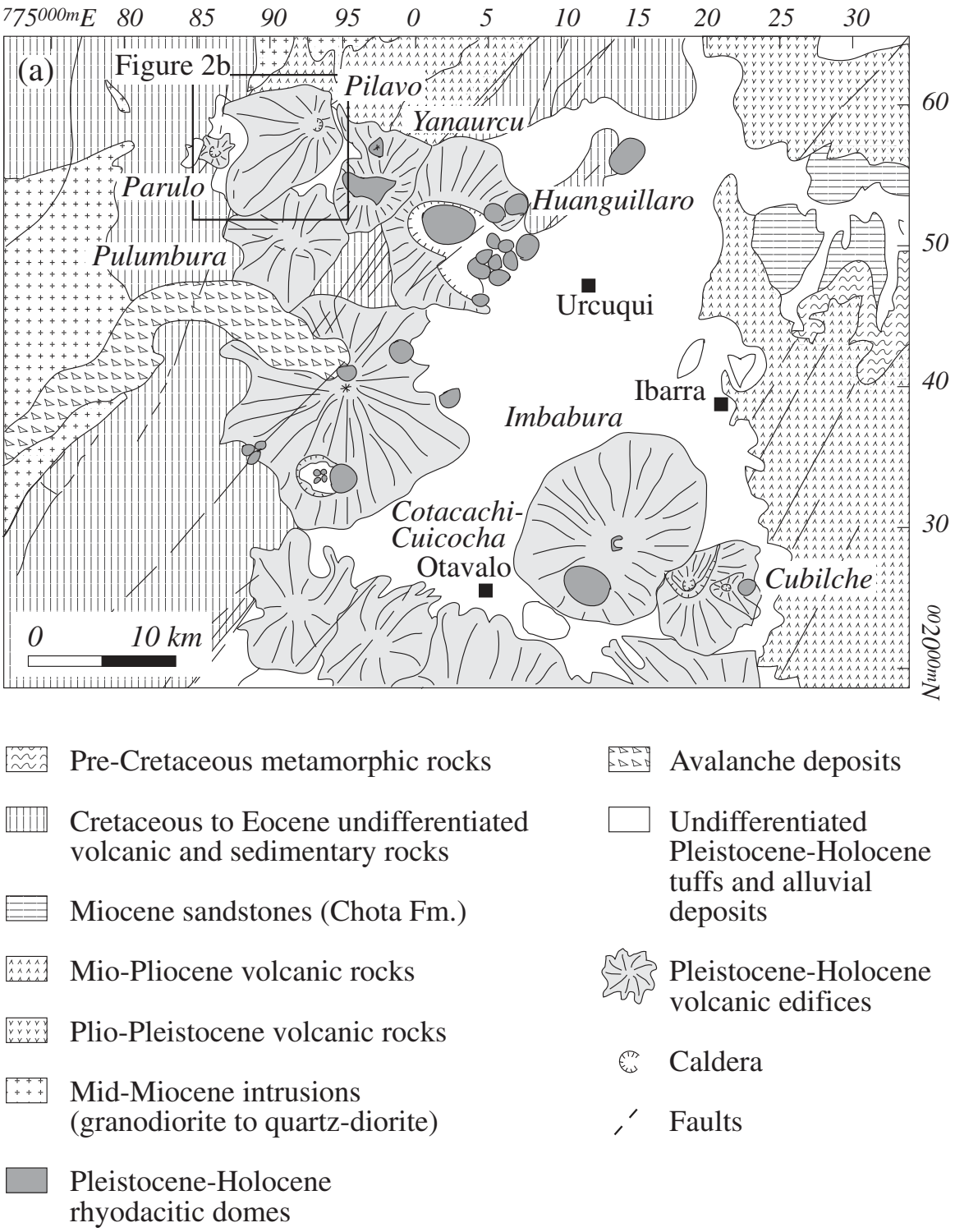

Fig. 2. (a) Simplified geological map of the volcanic complexes around Pilavo (modified after BGS & CODIGEM, 1999); (b) topographic map of Pilavo showing the locations of the samples investigated in this study. Lava flows are contoured. The earlier part of the volcanic edifice is indicated by the horizontally striped area. UTM coordinates (relative to zone 17N) are reported on both maps.

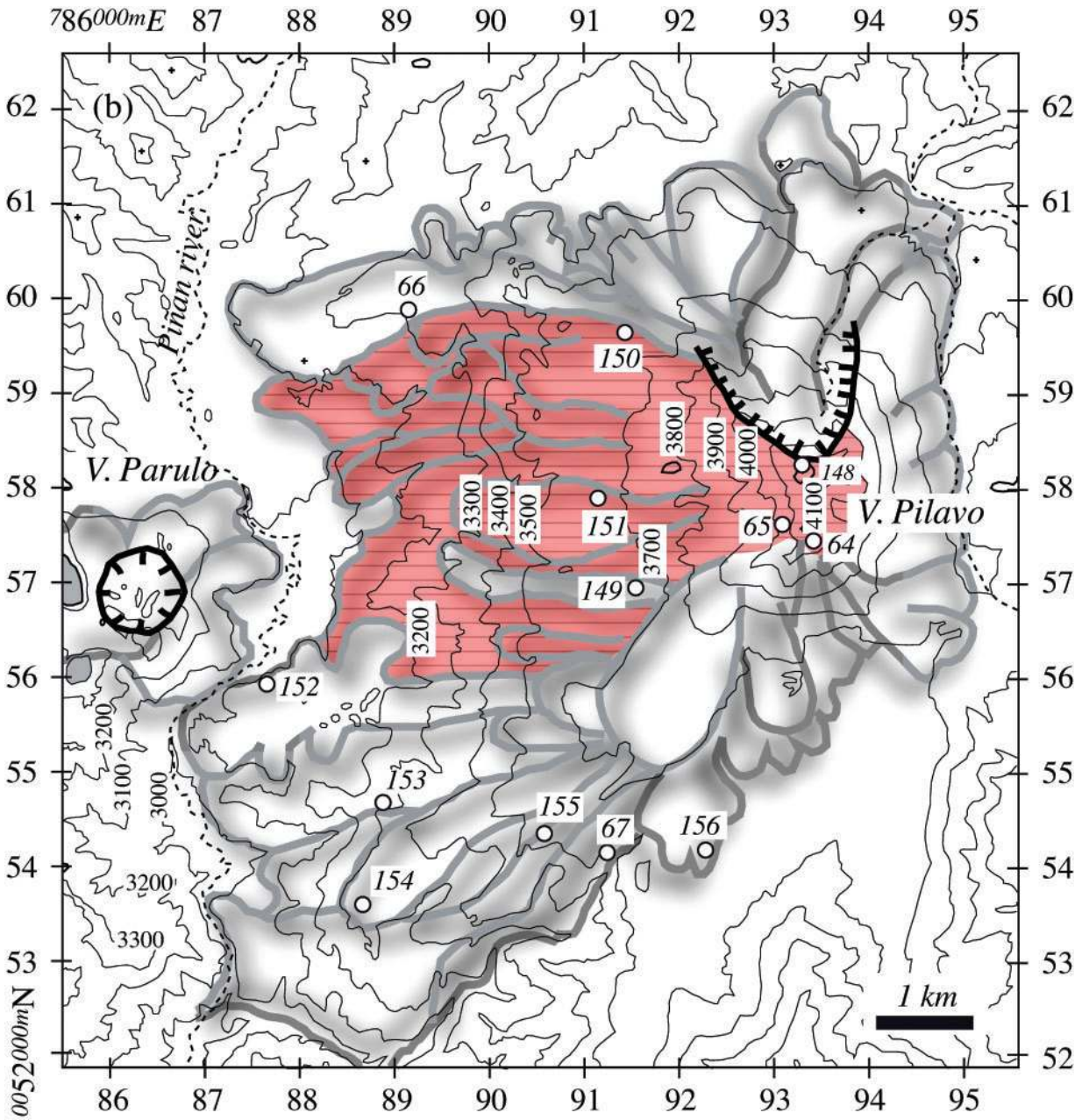

Fig. 2. Continued.

accreted to the continental margin during the Late Cretaceous, and of overlying Late Cretaceous to Tertiary (Eocene to Miocene) magmatic arcs (Vallejo *et al.*, 2006, 2009; Chiaradia, 2009). The exposed basement of Pilavo volcano (Fig. 2a) consists of Cretaceous marine sequences (Pilatón Unit) of volcanic sand- and siltstones as well as breccias derived from erosion of the Cretaceous Rio Cala basaltic arc (Chiaradia, 2009). These rock types are occasionally found as microcrystalline, millimeter-sized xenoliths in Pilavo lava flows, and are recrystallized to a fine-grained mosaic of epidote and amphibole (<200 μm crystal size).

Pilavo volcano consists of some 30 lava flows, reaching lengths up to 8 km (Fig. 2b), with a thickness of more than 40 m in many cases. Its morphology is closer to that of a shield than to that of a strato-volcano (Fig. 2b), with a total average basal diameter of about 8 km and a height of ~650 m. Pyroclastic deposits associated with Pilavo have

not been observed (either they never formed, or they were scarce or, if related to early activity, they were buried by later lava flows). NNE–SSW- and NW–SE-striking structures appear to have controlled the location of eruptive vents at Pilavo volcano, as well as at the neighbouring early Pleistocene andesitic Pulumbura volcano, the mid- to late Pleistocene Yanaurcu (andesite and dacite) and Huanguillaro (andesite to rhyodacite) composite stratovolcanoes (Fig. 2a). Normal, NNE–SSW-striking faults are also present in the area, affecting the Cretaceous–Eocene basement (Silante Fm.), but their relation to volcanic activity is unknown.

Pilavo blocky lava flows consist mainly of fresh, gray coloured, mostly non-vesicular, hornblende-, pyroxene-, ± plagioclase-phyric basaltic andesites to andesites, which are covered by 1–2 m of soil with intercalated distal Holocene pumice tephras (the youngest tephra, with an age of <8 ka, is from the Huanguillaro volcanic complex: Aguilera, 1998). The morphology of lava flows is fairly well preserved, as central flow waves, lateral levees, toes and tongues, can be recognized on topographic maps (Fig. 2b) and on aerial photographs. Flows have been affected slightly by glacial activity (at ~10–12 ka) at higher elevations, and the summit area shows a 1 km diameter depression open to the NNW, which could have been formed by glacial erosion, focused in the central vent area (summit). In contrast, Pilavo was not affected by the intense glacial erosion of the pleniglacial period (at 20–40 ka) like the adjacent Yanaurcu and Huanguillaro volcanoes. Based on these observations, Pilavo is older than 8 ka (the age of the youngest tephra from the Huanguillaro complex covering Pilavo) and probably younger than 20–40 ka.

Although Pilavo lava flows have similar petrographic characteristics (hornblende-bearing basaltic andesites), the morphology of the edifice suggests a three-stage development over a relatively short period of time, as follows.

(1) Eruption of several early lava flows mostly towards the west along a north–south- to NNE–SSW-oriented fissure located 4 km west of the summit (Fig. 2b: e.g. samples E05150, E05151).
(2) Eruption of abundant radiating lava flows (most of the collected samples) from the glacially eroded central vent located in the summit area (Fig. 2b). These lavas flowed around earlier flows mainly to the north, west and south, and surrounded the area of earlier flows towards the north and south of the fissure, constructing a lava flow-dominated edifice. This is the main building phase of Pilavo volcano.
(3) Eruption of the small dome–flow complex of Parulo, of similar petrography and immediately west of the Piñan river, to form Laguna Donoso by blocking the drainage with a lava flow (Fig. 2b). It is not clear yet if Parulo is earlier or later than Pilavo, based on field observations alone.

ANALYTICAL METHODS

Estimates of modal mineral abundances (Table 1) were obtained by image analysis carried out on thin sections with an estimated uncertainty (1σ) of ~10%. Thicknesses of amphibole phenocryst reaction rims were measured under the microscope on 1–3 polished thin sections per sample, using both transmitted and reflected light. Table 1 also reports the average thickness and corresponding standard deviation of the reaction rims measured around the entire amphibole population of each sample. Because we have measured reaction rim thickness on all the amphibole phenocrysts present in each thin section we assume that the effects of oblique sections through amphibole rims are similar for all samples. Although these measurements are subject to some uncertainty (preventing a correct estimate of ascent rates, which we therefore did not attempt to calculate), sample-to-sample variations are considered to be significant.

Microprobe analyses of pyroxene, amphibole, plagioclase, Fe–Ti-oxides and volcanic glass (Electronic Appendixes 1–5, available for downloading at http://www.petrology.oxfordjournals.org) were carried out at the Institute of Mineralogy and Geochemistry, University of Lausanne (Switzerland), using a JEOL 8200 microprobe equipped with five wavelength-dispersive spectrometers. Analytical conditions were: sample current 15 or 20–nA, acceleration voltage 15 kV, measuring time 10–30 s on peak, and half the time on the respective backgrounds depending on the element, and spot size of 1–5 μm depending on the element and mineral. Both natural and synthetic silicate, oxide, and sulfate standards were used for external calibration.

In situ trace element and REE analyses of volcanic glass, amphibole and clinopyroxene (Electronic Appendixes 5–7) were carried out on polished thin sections by laser ablation inductively coupled plasma mass spectrometry (LA-ICP-MS) using a Perkin Elmer ELAN 6100 DRC system equipped with a 193 nm excimer laser (Geolas) at the University of Lausanne. Operating conditions of the laser were: 8 Hz frequency, 100 mJ energy, 60 μm spot size. CaO contents determined by electron microprobe in the area of subsequent ablation with the laser were used for internal standardization by reference to an SRM612 NIST external standard. Raw data were reduced off-line using the LAMTRACE software (Jackson *et al.*, 1992; Longerich *et al.*, 1996; Jackson, 2008). The reproducibility (1σ) of the measured trace elements in the SRM612 standard was <10% for Ni and <5% for all other elements (Electronic Appendix 6).

Thirteen whole-rock samples (Table 2 and Fig. 2b) were analyzed for major and trace elements by X-ray

Table 1: Mineral modal abundances in volcanic rocks of Pilavo calculated from image analysis and average thickness of reaction rims around amphibole phenocrysts with its corresponding standard deviation

Sample:	E0506	E0506	E0506	E0506	E0514	E0514	E0515	E0515	E0515	E0515	E0515	E0515	E0515
Rock:	Andesite	Andesite	Andesite	Andesite	Andesite	Andesite	Basaltic andesite	Andesite	Basaltic	Andesite andesite	Andesite	Andesite	Andesite
amph (modal %)	4	3	13	12	2	10	5	11	17	3	4	2	17
cpx (modal %)	20	13	5	8	27	6	20	1	15	14	27	20	5
plag (modal %)*	39	80	25	15	55	22	39	45	15	15	27	23	18
mt (modal %)	5	2	4	3	3	4	5	2	5	5	5	5	2
gm (modal %)†	32	3	53	62	14	59	31	41	48	63	38	50	58
Average thickness of reaction rim around amphibole (μm)	130	183	44	28	80	75	183	96	72	90	68	90	18
n	31	12	39	73	21	44	26	168	248	22	69	65	43
1σ of thickness (μm)	103	78	29	7	33	53	39	55	38	40	44	42	3

*Includes microcrysts in the groundmass but not microlites (<150 μm).
†Includes glass and plagioclase-clinopyroxene microlites (<150 μm).
Estimated 1σ uncertainty for modal abundances is 10%. *n*, number of amphibole phenocrysts around which reaction rims were measured. amph, amphibole; cpx, clinopyroxene; plag, plagioclase; mt, magnetite; gm, groundmass.

fluorescence (XRF) at the University of Lausanne. The BHVO-1 basaltic standard was used for quality control. The 1σ uncertainties based on repeated measurements of this standard are <0·5% for all major elements (except MgO, 1·5%, and Na_2O, 3·3%; Table 2) and <1% for trace elements. REE and additional trace elements (e.g. Th, U, Ta, Cs, Hf) were measured by LA-ICP-MS on the fused glass beads used for major element XRF analysis (Table 2). Operating conditions of the laser were: 10 Hz frequency, 140 mJ energy, 120 μm spot size. CaO contents previously determined by XRF were used for internal standardization by reference to an SRM612 NIST external standard. Raw data were reduced off-line using the LAMTRACE software. For each sample 3–4 points were measured and results were then averaged. Uncertainties (1σ) between results of repeat points of the same sample were <10% for REE and <5% for the other trace elements analyzed, whereas the 1σ uncertainties of repeated measurements of the SRM612 NIST glass were <5% for all elements (Table 2).

All 13 whole-rocks were analyzed for their Sr, Nd and Pb isotopic compositions at the Department of Mineralogy, University of Geneva (Table 2). About 130 mg of powdered rock (<70 μm) were dissolved in closed Teflon vials for 7 days on a hot plate at 140°C with a mixture of 4 ml conc. HF and 1 ml HNO_3 15 M. The sample was then dried on a hot plate, and re-dissolved in 3 ml of 14 M HNO_3 in closed Teflon vials at 140°C and dried down again. Additionally we also analyzed Sr and Nd isotopes on a microdrilled amphibole phenocryst and its host groundmass (sample E05156) to check for possible disequilibrium between phenocrysts and groundmass. The analyzed material (*c.* 8 mg in both cases) was obtained by drilling a cylinder of *c.* 3 mm diameter out of a 350 μm thick thin section using a diamond microdrill.

Sr, Nd and Pb separation was carried out using cascade columns with Sr-spec, TRU-spec and Ln-spec resins following a modified method after Pin *et al.* (1994). Pb was further purified with an AG-MP1-M anion exchange resin in a hydrobromic medium. Pb, Sr and Nd isotope ratios were measured on a Thermo TRITON mass spectrometer on Faraday cups in static mode. Pb was loaded onto Re filaments using the silica gel technique and all samples (and standards) were measured at a pyrometer-controlled temperature of 1220°C. Pb isotope ratios were corrected for instrumental fractionation by a factor of 0·07% per a.m.u. based on more than 90 measurements of the SRM981 standard and using the standard values of Todt *et al.* (1996). External reproducibility of the standard ratios is 0·11% for $^{206}Pb/^{204}Pb$, 0·12% for $^{207}Pb/^{204}Pb$ and 0·20% for $^{208}Pb/^{204}Pb$.

Sr was loaded on single Re filaments with a Ta oxide solution and measured at a pyrometer-controlled temperature of 1480°C in static mode using the virtual amplifier design to cancel out biases in gain calibration among amplifiers. $^{87}Sr/^{86}Sr$ values were internally corrected for

Table 2: Geochemical and isotopic data for the Pilavo lavas investigated in this study

Sample:	E05064	E05065	E05066	E05067	E05148	E05149	E05150	E05151
Rock:	Andesite	Andesite	Andesite	Andesite	Andesite	Andesite	Bas. andesite	Andesite
SiO_2	57·57	56·07	56·07	56·42	56·04	57·37	54·17	56·54
TiO_2	0·73	0·71	0·76	0·81	0·76	0·75	0·69	0·66
Al_2O_3	17·66	17·85	17·43	17·22	17·22	16·81	17·1	18·17
$Fe_2O_{3(tot)}$	8·29	9·13	8·93	8·07	8·85	7·82	9·33	8·63
MnO	0·15	0·16	0·15	0·13	0·16	0·13	0·17	0·15
MgO	3·25	3·73	3·58	3·3	3·52	3·1	3·8	3·45
CaO	7·41	7·97	7·7	7·23	7·68	7·05	8·23	7·65
Na_2O	3·16	3·01	2·95	3·15	3·05	3·26	2·9	3·04
K_2O	1·77	1·13	1·86	2·36	1·67	2·36	1·38	0·95
P_2O_5	0·28	0·23	0·28	0·32	0·27	0·33	0·25	0·22
LOI	0·02	−0·15	0·28	0·45	0·00	0·08	0·21	0·35
Total	100·3	99·81	99·99	99·55	99·25	99·12	98·26	99·78
Rb	32·3	17·1	29·8	42·9	30·9	44·1	22·2	14·2
Sr	907	666	1135	1298	904	1226	901	700
Y	16·5	16·2	18·5	16·6	18·3	15·9	18·4	15·5
Zr	133	80	156	222	131	206	108	85
Nb	4·0	3·2	4·1	5·4	4·0	5·2	3·4	3·1
Cs	0·6	0·4	0·8	1·1	0·4	1·1	0·6	0·6
Be	2·2	1·7	2·2	3·3	0·8	1·4	1·3	1·1
Ba	1119	734	1412	1465	1019	1439	968	648
Hf	2·8	2·0	3·2	4·8	2·6	3·7	1·9	1·8
Ta	0·3	0·3	0·3	0·4	0·2	0·2	b.d.l.	0·1
Pb	8·6	7·6	9·5	12·3	7·0	12·0	8·0	6·0
Th	8·4	4·5	15·2	14·6	7·4	11·9	8·0	4·1
U	2·3	1·2	3·6	3·5	2·1	3·3	2·4	1·2
Sc	21·7	23·8	22·8	22·1	21·3	18·2	23·1	21·0
V	138	161	168	159	241	174	203	183
Cr	4	13	6	17	6	14	11	12
Ni	4	6	6	10	8	12	9	10
Cu	56	48	37	37	63	57	44	33
Co	27	25	19	19	22	18	25	28
Zn	60	68	77	76	90	86	89	87
La	27·7	14·6	43·9	50·1	24·2	42·6	25·8	13·7
Ce	50·6	26·7	72·5	85·9	44·6	78·3	46·6	25·8
Pr	5·9	3·4	8·3	10·2	5·3	9·2	5·4	3·3
Nd	23·8	14·9	32·8	41·5	20·9	34·6	20·4	13·4
Sm	4·6	3·1	5·7	7·2	4·1	6·1	3·8	2·9
Eu	1·3	1·0	1·5	1·8	1·3	1·7	1·0	0·8
Gd	3·5	3·2	4·2	5·7	3·2	4·6	3·2	2·7
Tb	0·54	0·47	0·58	0·66	0·43	0·52	0·45	0·37
Dy	3·3	2·9	3·7	3·8	2·9	3·1	2·7	2·5
Ho	0·64	0·61	0·71	0·72	0·57	0·52	0·54	0·48
Er	1·78	1·85	1·98	1·86	1·67	1·37	1·48	1·41
Tm	0·26	0·26	0·31	0·25	0·21	0·2	0·22	0·19
Yb	1·83	1·75	1·94	1·48	1·29	1·38	1·44	1·3
Lu	0·26	0·26	0·30	0·24	0·24	0·19	0·22	0·20
Mg-no.	0·44	0·45	0·44	0·45	0·44	0·44	0·45	0·44
$^{87}Sr/^{86}Sr$	0·703867	0·703765	0·703874	0·703898	0·703848	0·703884	0·703823	0·703859
$^{143}Nd/^{144}Nd$	0·512934	0·512952	0·512933	0·512931	0·512923	0·512927	0·512939	0·51295
ε_{Nd} (CHUR)	5·8	6·1	5·8	5·7	5·6	5·6	5·9	6·1
$^{206}Pb/^{204}Pb$	19·024	19·059	19·065	19·027	19·021	19·038	19·050	19·028
$^{207}Pb/^{204}Pb$	15·579	15·600	15·589	15·594	15·579	15·598	15·586	15·572
$^{208}Pb/^{204}Pb$	38·631	38·750	38·760	38·724	38·692	38·742	38·738	38·667

(continued)

Table 2: Continued

Sample:	E05152	E05153	E05154	E05155	E05156	E05156	E05156
Rock:	Bas. andesite	Andesite	Andesite	Andesite	Andesite	Amphibole	Groundmass
SiO_2	53·74	56·94	56·79	56·59	57·47		
TiO_2	0·75	0·77	0·76	0·77	0·77		
Al_2O_3	16·63	17·13	17·01	17·02	16·6		
$Fe_2O_{3(tot)}$	8·92	8·48	8·28	8·53	7·85		
MnO	0·16	0·14	0·14	0·15	0·13		
MgO	3·56	3·36	3·25	3·42	3·2		
CaO	7·48	7·43	7·27	7·37	7·11		
Na_2O	2·87	3·16	3·1	3·06	3·14		
K_2O	1·86	1·89	2·1	1·89	2·37		
P_2O_5	0·28	0·29	0·31	0·29	0·33		
LOI	2·76	0	0·32	0·31	0·36		
Total	99·06	99·62	99·35	99·42	99·41		
Rb	28·4	34·2	40·5	35·3	40·48		
Sr	1344	983	1048	951	1188		
Y	19·9	16·7	16·3	17·0	15·0		
Zr	217	148	167	145	138		
Nb	4·9	4·2	4·5	4·3	4·6		
Cs	1·0	0·7	1·0	0·9	1·0		
Be	2·4	1·3	2·5	1·7	4·4		
Ba	1777	1170	1288	1136	1196		
Hf	3·9	2·9	3·2	2·9	3·8		
Ta	0·2	0·2	0·3	0·2	0·2		
Pb	14·0	6·0	10·0	8·0	10·8		
Th	23·9	9·1	10·6	9·3	11·8		
U	6·0	2·5	2·9	2·5	3·2		
Sc	22·0	19·8	19·1	20·4	18·1		
V	203	191	185	190	181		
Cr	11	5	4	6	19		
Ni	10	9	9	9	14		
Cu	29	59	45	64	45		
Co	24	22	21	22	23		
Zn	99	91	90	90	86		
La	66·7	30·7	35·6	30·2	42·2		
Ce	116·4	56·2	65·0	56·3	79·6		
Pr	12·2	6·6	7·5	6·6	9·4		
Nd	45·3	26·4	30·1	26·0	37·4		
Sm	7·3	4·9	5·3	4·4	6·3		
Eu	2·0	1·4	1·4	1·3	1·7		
Gd	5·0	4·1	4·2	4·0	4·3		
Tb	0·64	0·47	0·51	0·5	0·56		
Dy	3·6	3·0	2·9	3·0	2·9		
Ho	0·65	0·57	0·57	0·56	0·54		
Er	1·73	1·58	1·42	1·55	1·39		
Tm	0·25	0·22	0·21	0·22	0·18		
Yb	1·68	1·34	1·37	1·35	1·22		
Lu	0·25	0·20	0·20	0·22	0·19		
Mg-no.	0·44	0·44	0·44	0·44	0·45		
$^{87}Sr/^{86}Sr$	0·703924	0·703873	0·703881	0·703864	0·703893	0·703889	0·703888
$^{143}Nd/^{144}Nd$	0·512926	0·512926	0·512925	0·512929	0·512930	0·512948	0·512954
ε_{Nd} (CHUR)	5·6	5·6	5·6	5·7	5·7	6·0	6·2
$^{206}Pb/^{204}Pb$	19·137	19·023	19·025	19·072	19·023		
$^{207}Pb/^{204}Pb$	15·598	15·577	15·578	15·618	15·583		
$^{208}Pb/^{204}Pb$	38·850	38·694	38·708	38·804	38·694		

(continued)

Table 2: Continued

Sample:	BHVO-1		SRM612	
Rock:	Basalt standard (average, $n=8$)	1σ	Glass standard (average, $n=28$)	1σ
SiO_2	49·60	0·08		
TiO_2	2·71	0·00		
Al_2O_3	13·63	0·04		
$Fe_2O_{3(tot)}$	12·22	0·01		
MnO	0·17	0·00		
MgO	7·21	0·11		
CaO	11·39	0·03		
Na_2O	2·40	0·08		
K_2O	0·55	0·00		
P_2O_5	0·28	0·00		
LOI	0			
Total	100·21	0·13		
Rb			31·57	0·69
Sr			76·67	1·23
Y			38·51	0·75
Zr			36·23	0·72
Nb			38·32	0·73
Cs			41·92	0·84
Be			37·99	1·53
Ba			38·00	0·67
Hf			35·00	0·71
Ta			40·04	0·85
Pb			39·22	0·59
Th			37·48	0·73
U			37·40	0·77
Sc			41·33	0·77
V			39·49	0·45
Cr	299·20	4·76		
Ni	130·20	1·10		
Cu			36·96	0·61
Co			35·50	0·58
Zn	106·00	1·00		
La			36·01	0·65
Ce			38·61	0·68
Pr			37·41	0·75
Nd			35·48	0·77
Sm			36·97	0·71
Eu			34·67	0·67
Gd			37·20	0·63
Tb			36·16	0·64
Dy			36·21	0·68
Ho			38·13	0·80
Er			37·68	0·78
Tm			37·80	0·81
Yb			40·22	0·88
Lu			37·96	0·81

Also reported are the averages and standard deviations of analyses obtained on the BHVO-1 basalt standard (XRF analyses) and of the SRM612 glass standard (LA-ICP-MS analyses) under the same analytical conditions as used for the analysis of whole-rocks (see text). Major elements, Cr, Ni and Zn were analyzed by XRF; all other elements by LA-ICP-MS. b.d.l., below detection limit.

fractionation using a $^{88}Sr/^{86}Sr$ value of 8·375209. Raw values were further corrected for external fractionation by a value of +0·03‰, determined by repeated measurements of the SRM987 standard ($^{87}Sr/^{86}Sr = 0·710250$). External reproducibility of the $^{87}Sr/^{86}Sr$ ratio for the SRM987 standard is 7 ppm. Nd was loaded onto double Re filaments with 1 M HNO_3 and measured in static mode with the virtual amplifier design. $^{143}Nd/^{144}Nd$ values were internally corrected for fractionation using a $^{146}Nd/^{144}Nd$ value of 0·7219 and the ^{144}Sm interference on ^{144}Nd was monitored on the mass ^{147}Sm and corrected using a $^{144}Sm/^{147}Sm$ value of 0·206700. External reproducibility of the JNdi-1 standard (Tanaka *et al.*, 2000) is <5 ppm.

PETROGRAPHY AND MINERAL CHEMISTRY

Pilavo andesitic lavas are porphyritic with phenocrysts of amphibole, clinopyroxene and, especially in the least evolved rocks, plagioclase. Sizes of amphibole and clinopyroxene phenocrysts range from several hundreds of micrometers to almost 1 cm in some cases, whereas plagioclase phenocrysts range from a few hundreds of micrometers to a few millimeters. The groundmass consists of plagioclase and clinopyroxene microlites (<150 μm) and fresh glass. The abundance of amphibole phenocrysts systematically increases and that of plagioclase systematically decreases with increasing content of incompatible elements in the whole-rock (see below). The amphibole-rich (plagioclase-poor) samples also contain quartz xenocrysts surrounded by glass and acicular clinopyroxene coronas (see below). In some samples (E05150) quenched mafic enclaves in the basaltic andesite lava display a fluidal texture consisting of plagioclase and pyroxene microlites (<150 μm).

Pyroxene

Clinopyroxene is virtually the only pyroxene present, with orthopyroxene found only in two cases (as a core replaced by clinopyroxene in a corona around a quartz xenocryst and as a reaction rim assemblage around an amphibole phenocryst). We have distinguished five textural types of clinopyroxene: (1) large (millimeter- to centimeter-sized) relic phenocrysts surrounded by a corona of amphibole (Fig. 3a); (2) isolated phenocrysts (Fig. 3b) with either concentric or sector zoning (hundreds of micrometers to several millimeters) and idiomorphic to sub-idiomorphic shapes; (3) clots of several clinopyroxene crystals (hundreds of micrometers to several millimeters; Fig. 3c) with either sector or concentric zoning; (4) clots of several clinopyroxene crystals in association with amphibole ± plagioclase (hundreds of micrometers to several millimeters; Fig. 3d); (5) products of the reactions of melt with amphibole (Fig. 3f) or quartz xenocrysts (Fig. 3j–l).

All these textural types have augitic compositions, except for the acicular clinopyroxenes surrounding the glass coronas of quartz xenocrysts, which are diopsidic (Electronic Appendix 1). Excluding sector-zoned clinopyroxene phenocrysts, whose compositional zoning may be the result of rapid growth, and the clinopyroxenes that are related to melt–amphibole and melt–quartz reactions, relic clinopyroxene phenocrysts surrounded by a corona of amphibole display the highest Na and Al^{vi} contents, followed by unzoned clinopyroxene of the most primitive rock (E05065), by clinopyroxene associated with amphibole and finally by clinopyroxene in clots (Fig. 4a). In particular, relic clinopyroxene phenocrysts have systematically higher Na and Al^{vi} contents than all other clinopyroxene types within each sample, suggesting that they were formed under higher pressure conditions. Concentrically zoned clinopyroxene, both in clots and in isolated grains, usually displays normal zoning with more magnesian cores with respect to rims. The various textural types of clinopyroxene defined above may coexist in the same sample.

REE patterns of clinopyroxene are hump-shaped with an increasing slope from La to Nd and then a slightly decreasing slope from Sm to Lu, with no or very minor Eu negative anomalies (Fig. 4b). Clinopyroxene trace element compositions (Electronic Appendix 6) display systematic changes with host-rock composition. For example, Sr, Sr/Y, Dy/Yb, and La/Yb of clinopyroxene increase with the chemical evolution of the host-rock (e.g. increasing K_2O of whole-rock: Fig. 4c and d).

Amphibole

We have distinguished three textural types of amphibole phenocryst: (1) amphibole with two or three concentric growth zones separated by a layer of fine-grained Fe-oxides (Fig. 3f); (2) amphibole similar to the type above (two or three concentric growth zones separated by a layer of fine-grained Fe-oxides) overgrown around a single large relic clinopyroxene phenocryst or a cluster of several clinopyroxene phenocrysts (Fig. 3a); (3) optically homogeneous amphibole isolated (Fig. 3g) or in association with clinopyroxene (Fig. 3d). Amphibole types (1) and (2) occur only in the most evolved rocks, whereas type (3) occurs in all the rocks of Pilavo.

The three textural types of amphibole phenocrys are surrounded, when in contact with the groundmass, by variably thick reaction rims of two types (Fig. 3e–i): (1) opacite rims (Fig. 3g) and/or (2) gabbroic (plagioclase–pyroxene–Fe oxide) rims (Fig. 3e, f and h). Gabbroic rims are usually considered the result of amphibole–melt reaction during decompression (e.g. Rutherford & Hill, 1993). The thickness of the gabbroic rims, as well as the size and shape of the crystals in these rims, varies systematically from sample to sample (from a few tens to a few hundreds of micrometers; Fig. 3e–h: see below) and even for different amphiboles within the same thin section. Crystals in the reaction rims may be more or less elongated (to acicular)

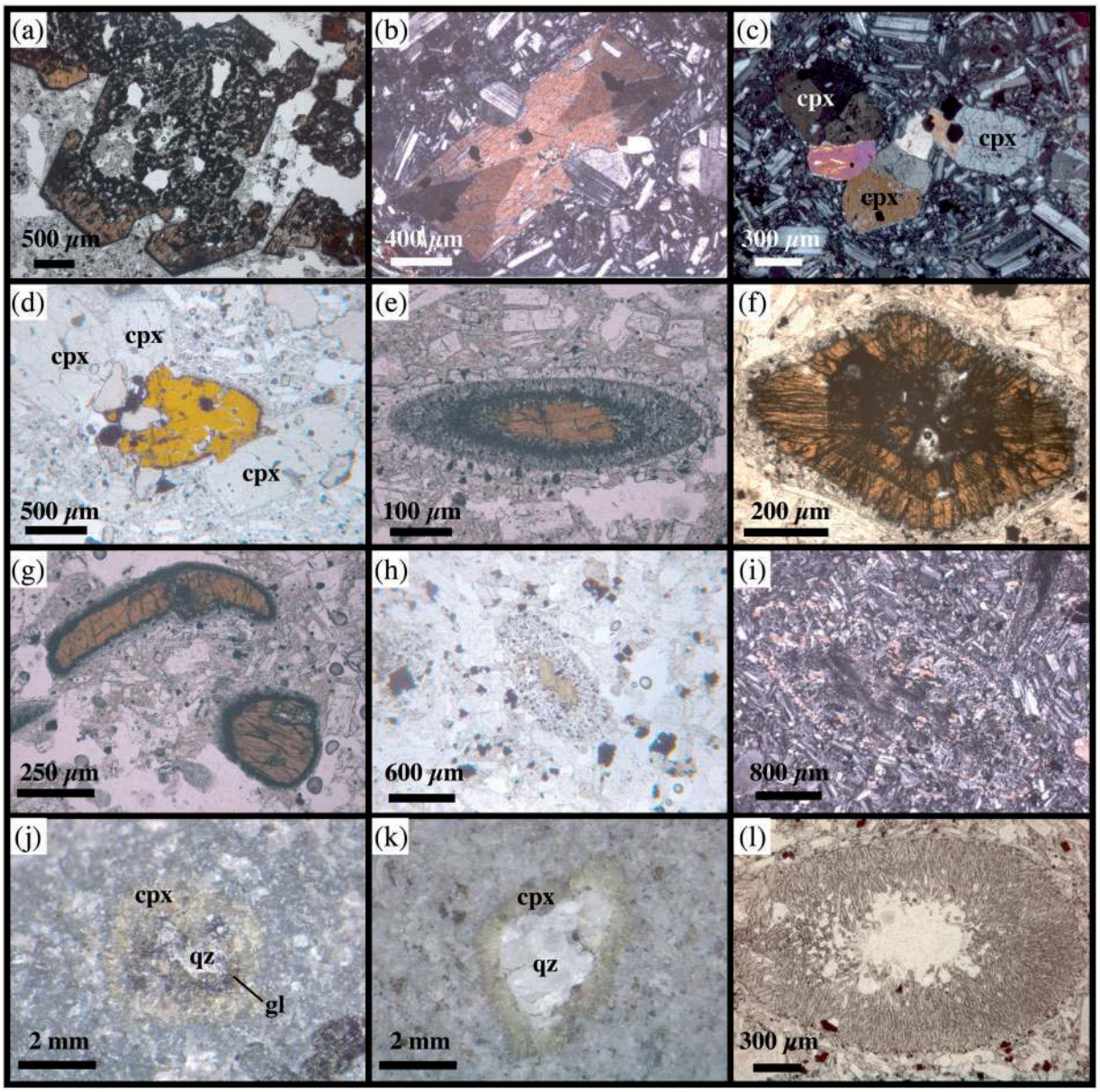

Fig. 3. Photomicrographs of Pilavo lava textures. (a) Amphibole megacryst with a poikilitic core of high Al_2O_3-clinopyroxene and Fe-oxides (sample E05156: parallel Nicols). (b) Sector-zoned clinopyroxene phenocryst (sample E05156: crossed Nicols). (c) Clinopyroxene clot (sample E05150: crossed Nicols). (d) Amphibole and clinopyroxene (cpx) clot (sample E05066: parallel Nicols). (e) Rounded amphibole surrounded by a fine-grained gabbroic rim and a corona of coarse-grained clinopyroxene (sample E05151: parallel Nicols). (f) Optically multi-zoned amphibole with gabbroic rim (sample E05153: parallel Nicols). (g) Amphibole with opacite rim (sample E05067: parallel Nicols). (h) Amphibole with thick gabbroic rim (sample E05064: parallel Nicols). (i) Amphibole completely replaced by pyroxene–plagioclase ± oxides (sample E05065: crossed Nicols). (j) Corona texture around quartz xenocryst (sample E05067: binocular microscope). From core to rim: white-transparent (quartz, qz), blackish (glass, gl), light grey (clinopyroxene, cpx). (k) Clinopyroxene (cpx) corona texture around quartz (qz) xenocryst (sample E05067: binocular microscope). (l) Acicular clinopyroxene in corona texture around quartz xenocryst (accidentally removed during thin section preparation; parallel Nicols: sample E05067).

and fairly large (up to a few tens of micrometers). In some cases no residual amphibole is left (Fig. 3i). In a few cases amphibole phenocrysts are surrounded by a corona of equant clinopyroxene crystals (Fig. 3e), which in turn surround the rim of plagioclase–pyroxene–oxide aggregate.

Pilavo amphiboles can be classified as ferri-tschermakite to magnesio-hastingsite (Electronic Appendix 2) according to the scheme of Leake *et al.* (1997). They are characterized by roughly constant Al^{vi} with variable Al^{iv}, suggesting the lack of pressure-sensitive Al-Tschermaks

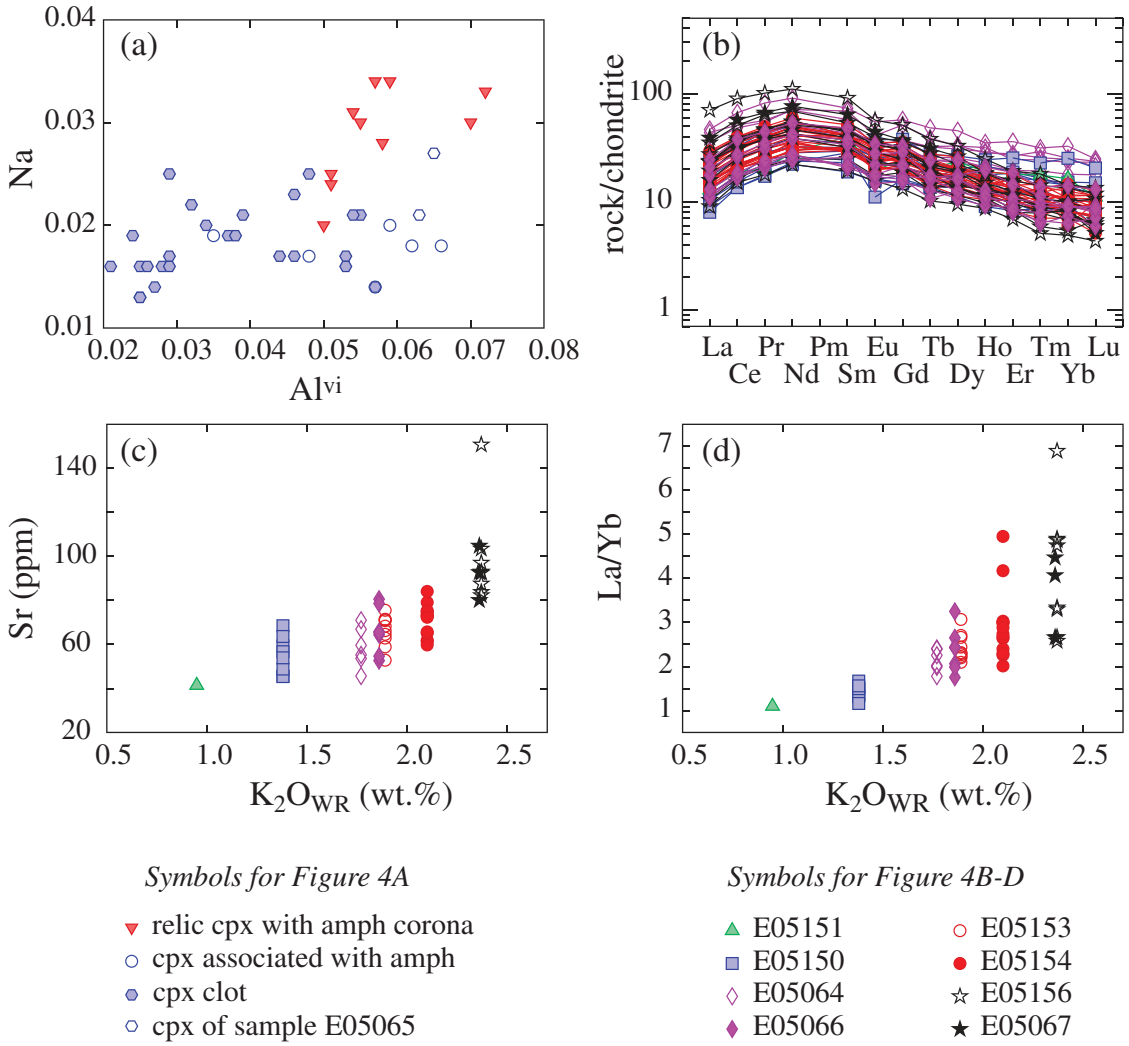

Fig. 4. Clinopyroxene chemistry: (a) Na vs Al^{vi} plot for clinopyroxenes in Pilavo lavas showing that clinopyroxene relict crystals surrounded by amphibole coronas and clinopyroxene associated with amphiboles have generally the highest Na and Al^{vi} contents; (b) REE patterns for Pilavo clinopyroxenes; (c, d) Sr and La/Yb variations of Pilavo clinopyroxenes vs K_2O contents of the corresponding host whole-rocks.

exchange. In contrast, they display a broadly positive correlation between $(Na+K)_A$ and Al^{iv} suggesting a *T*-dependent edenite exchange. Therefore, the variable Al_2O_3 contents of the Pilavo amphiboles reflect *T* rather than *P* changes. None the less, the overall high-Al_2O_3 ($\geq$12 wt %) Pilavo amphiboles are similar in composition to the high-Al_2O_3 amphiboles of Mount St. Helens, which are considered to have crystallized at depths >15 km (Thornber *et al.*, 2008).

REE patterns of amphiboles are similar to those of clinopyroxene, with slope increasing from La to Nd and slightly decreasing from Sm to Lu and no significant Eu negative anomalies (Fig. 5a; Electronic Appendix 7). REE concentrations of amphibole are comparable with to slightly lower than those of clinopyroxene (Figs 4b and 5a; Electronic Appendixes 6–7). Like clinopyroxene, amphibole displays systematic changes with the chemistry of the host-rock; for example, K_2O, Sr and Rb increase with increasing whole-rock K_2O (Fig. 5b).

Amphibole with optically distinct growth zones displays Mg-number ($\pm TiO_2$, K_2O) increase and Na_2O decrease (Fig. 5c) from the core to the adjacent outer zone. Rims can be either more or (slightly) less magnesian than the preceding zone, but are generally more magnesian than cores (Fig. 5c). Optically homogeneous amphiboles are generally richer in Mg than cores of zoned amphiboles and often as Mg-rich as their rims (compare E05153 and E05066: Fig. 5c and d). They are characterized by a slight decrease of Mg-number and K_2O and by an increase of TiO_2 from core to rim (Fig. 5d). Amphiboles with variably Mg-rich cores may also coexist in the same sample. Pilavo amphiboles, especially the rims of crystals from the most

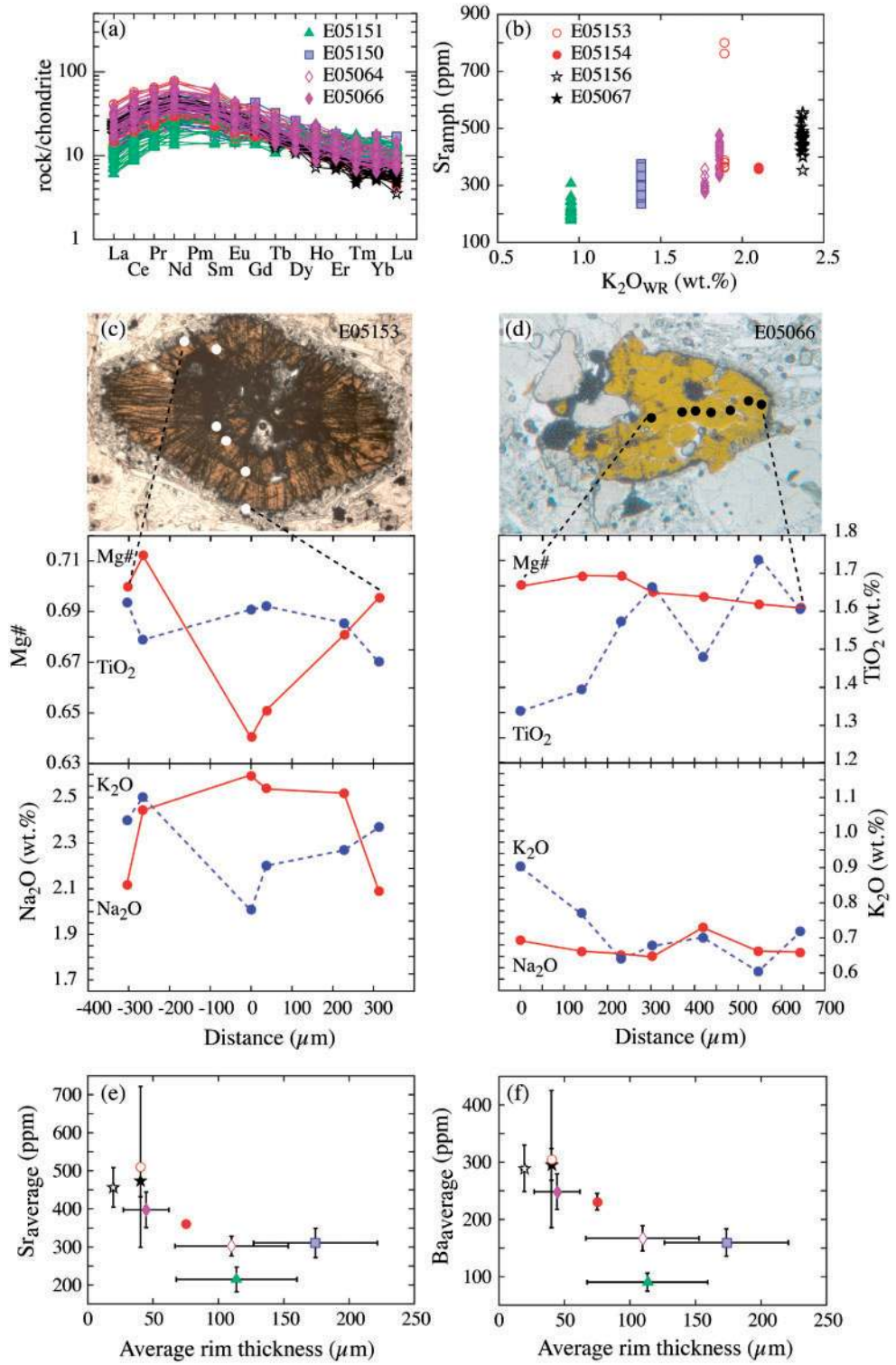

Fig. 5. (a) REE patterns of Pilavo amphiboles. (b) Sr variations of Pilavo amphiboles vs K_2O contents of the corresponding host whole-rocks. (c, d) Mg-number, TiO_2, K_2O and Na_2O concentration profiles in optically zoned and unzoned amphiboles from Pilavo lavas. Reported distances (μm) are always from the core (0 μm). (e, f) Correlations between average reaction rim thickness around amphiboles and their average Sr and Ba contents (error bars represent the associated standard deviations).

evolved rocks, can have high F contents, ranging from 0·1 to 2·7 wt % (fluor-magnesio-hastingsite).

The average thickness of the reaction rims of the amphibole population in each thin section (Table 2) shows a broad inverse correlation with average incompatible element content of the amphibole (Fig. 5e and f).

Plagioclase

We have distinguished three texturally different types of plagioclase, as follows.

(1) Plagioclase phenocrysts (up to a few millimeters in size) consisting almost entirely of a heavily sieve-textured core, which is corroded and overgrown by a thin clear rim (Fig. 6a). The cores of these plagioclase phenocrysts are anorthite-rich (An>80 and up to An92) with the sieve-filling plagioclase being $An_{35–45}$ (Fig. 6a and b; Electronic Appendix 3). The clear outer rim, with concentric zoning, is usually An-poorer than the core (Fig. 6a; Electronic Appendix 3).
(2) Oscillatory zoned phenocrysts (300–600 μm) with poorly to non-sieved cores characterized by high anorthite contents ($An_{80–85}$) and a thin rim with lower anorthite content.
(3) Microcrysts (150–300 μm) in the matrix without sieved cores, characterized by a strong anorthite decrease from core to rim (Fig. 6b and c) and usually less anorthitic than phenocrysts.

Plagioclase displays systematic chemical changes with the composition of the host-rock. In particular, the maximum Sr contents of plagioclase are positively correlated with increasing evolution of the host-rocks (e.g. increasing K_2O, Sr and Th: Fig. 6d), despite the fact that Sr lacks any correlation with plagioclase anorthite content in our samples.

Fe–Ti oxides

Titanomagnetite occurs within amphibole (Fig. 7a), clinopyroxene (Fig. 7b) and, more rarely, plagioclase, and, to the greatest extent, as single pheno- and microcrysts in the groundmass. Titanomagnetite in amphibole phenocrysts is often associated (in contact) with hemoilmenite (Fig. 7a), whereas ilmenite has never been found within clinopyroxene and plagioclase phenocrysts or in the groundmass, except as exsolution lamellae.

Compositional variations of groundmass magnetite result from variations in the ulvöspinel and combined magnetite–magnesioferrite components, whereas the combined spinel–hercynite component remains low (~3%). In contrast, magnetite included in amphibole and clinopyroxene phenocrysts is characterized by an increasing spinel–hercynite component at the expense of ulvöspinel and magnetite–magnesioferrite components. The spinel and hercynite components are highest in the magnetite hosted by amphibole, in which MgO and Al_2O_3 can reach concentrations up to 11 wt % (Fig. 7c; Electronic Appendix 4). Also, hemoilmenite has high contents of MgO (up to 8 wt %) and Al_2O_3 (up to 3·5 wt %; Electronic Appendix 4).

Application of the magnetite–ilmenite thermometer and oxygen barometer [using the ILMAT software of Lepage (2003)] for the magnetite–hemoilmenite pairs of the amphibole phenocrysts [which have all passed the equilibrium test of Bacon & Hirschmann (1988)] yields temperatures ranging between 850 and 900°C, with one pair yielding a significantly higher temperature of 975°C (Fig. 7d; Electronic Appendix 4). Oxygen fugacities calculated from these pairs are high to very high, ranging from NNO + 1·5 to NNO + 3·3, where NNO is the nickel–nickel oxide buffer.

Quartz xenocrysts

A typical textural feature of only the most evolved Pilavo rocks is the occurrence of oval zoned globules (Fig. 3j–l), sub-millimeter to several millimeters in size, consisting of (1) an outer zone of coarse and equant crystals of clinopyroxene followed inward by (2) a zone of acicular clinopyroxene crystals growing radially inwards in a glass groundmass passing to (3) pure glass and finally to (4) quartz. Some globules consist entirely of plagioclase and clinopyroxene crystals with interstitial glass. In other cases the globule is completely occluded by acicular clinopyroxene crystals growing radially from the rim towards the core of the globule. These textures are identical to the corona textures around quartz xenocrysts in basaltic lavas described by Sato (1975). Acicular clinopyroxene in the globules has a diopsidic composition (Electronic Appendix 1) whereas equant clinopyroxene on the rim of the globules is augitic like the clinopyroxene in the lava and may surround a corroded core of orthopyroxene.

The glass of coronas from samples E05066 and E05155 (Electronic Appendix 5) has high SiO_2 (73–80 wt %), Al_2O_3 (8·6–9·3 wt %), K_2O (4·6–5·7 wt %) and Na_2O (1·9–2·8 wt %), and low FeO (<2 wt %), MgO (<0·1 wt %) and CaO (<0·3 wt %), similar to glass compositions in other coronas around quartz xenocrysts (e.g. Sato, 1975). All major elements (except the most compatible ones such as MgO, FeO plus TiO_2) display negative correlations with SiO_2. REE and incompatible element spectra of the glass of the globules are similar to those of the whole-rocks (Fig. 8a and b), although they are poorer in most incompatible elements. The only elements with concentrations in the glass higher than in the whole-rock are Rb, Cs, Pb and K (see also Sato, 1975). Glasses in the corona textures contain significant amounts of B (7–23 ppm) and F (1000–2000 ppm) (Electronic Appendix 5).

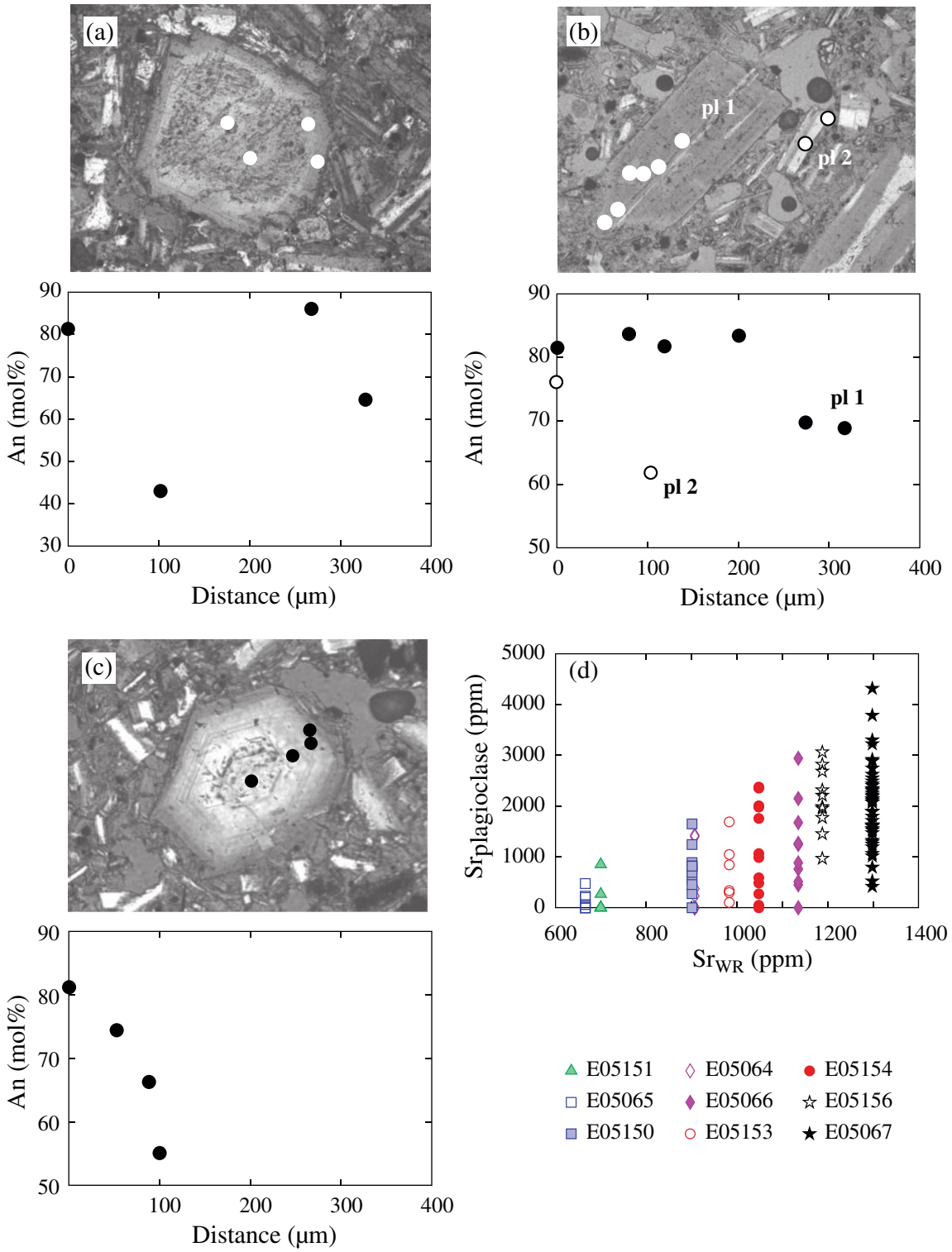

Fig. 6. Anorthite zoning of plagioclase phenocrysts for large phenocrysts with intensely sieved cores (a) characterized by albite-rich fillings of the sieves ($An_{30–40}$) (sample E05065), phenocrysts with weakly sieved cores (b) (sample E05067), and microcrysts in the groundmass (b and c) (sample E05067); (d) variations of Sr in plagioclase with whole-rock Sr content.

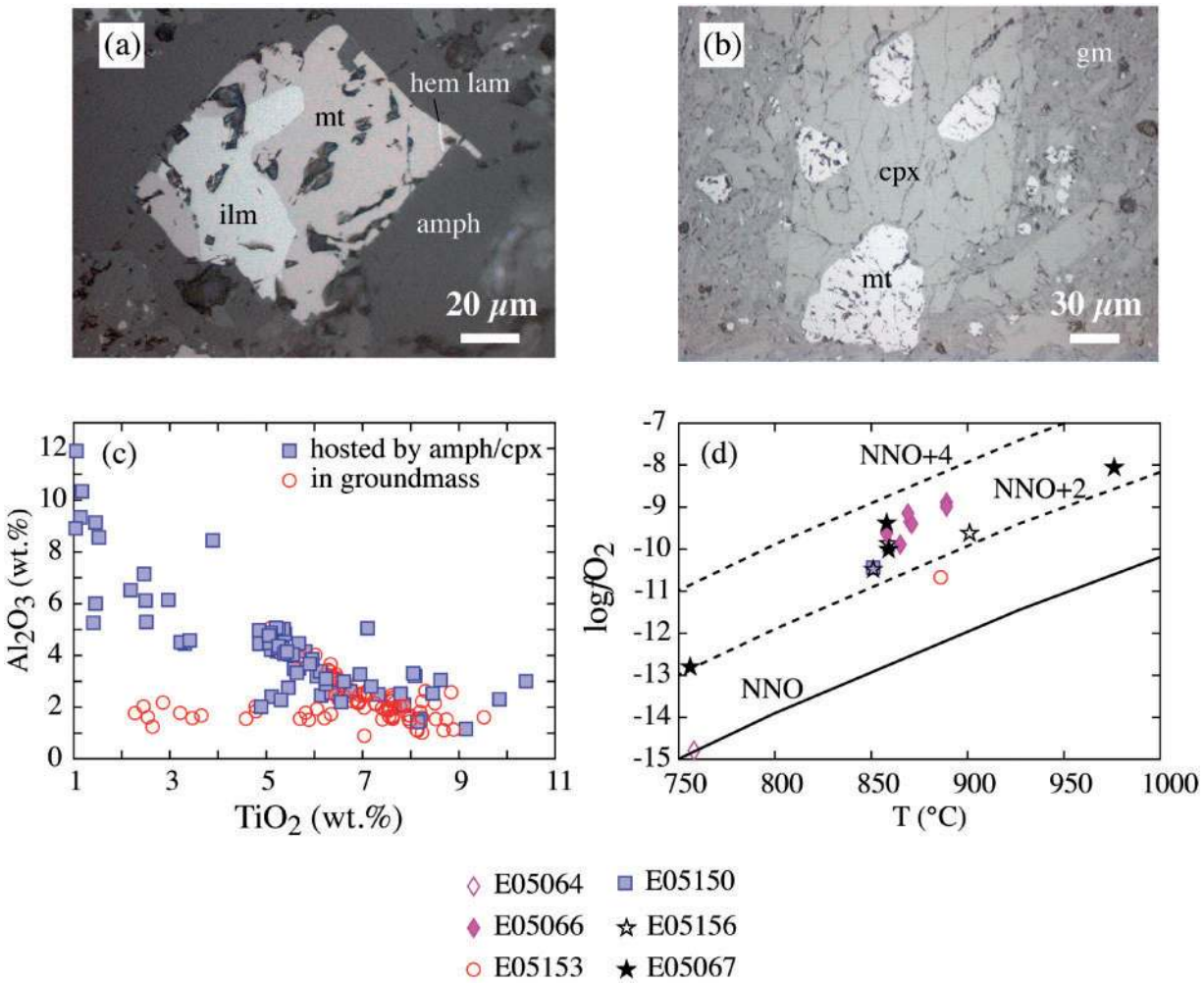

Fig. 7. Reflected light photomicrographs of Fe-oxide textures in Pilavo lavas. (a) Magnetite (mt)–hemoilmenite (ilm) association within amphibole (amph) phenocryst (sample E05156); (b) magnetite (mt) hosted by clinopyroxene (cpx) (sample E05066); (c) Al_2O_3 vs TiO_2 variations for Pilavo magnetites; (d) fO_2–T plot for the magnetite–hemoilmenite pairs within amphibole and for the magnetite–ilmenite pair of the groundmass (sample E05153) obtained using the ILMAT software of Lepage (2003) and ulvöspinel and ilmenite molar proportions calculated according to Lindsley & Spencer (1982). The two points yielding low T (~750°C) correspond to non-equilibrium magnetite with lamellar ilmenite exsolution in the groundmass. All others are equilibrium pairs hosted by amphibole.

GEOCHEMISTRY

Major, trace and rare earth elements

The Pilavo lavas are medium- to high-K basaltic andesites and low-SiO_2 andesites (Fig. 9a) with only a small range in major element composition (SiO_2 = 54–57·5 wt %, MgO = 3·1–3·8 wt %, Fe_2O_3 = 7·8–9·3 wt %; Table 2) in contrast with the medium-K high-SiO_2 andesites and dacites of the other frontal volcanoes of Ecuador (e.g. Pululahua, Pichincha; Fig. 9a). Additionally, the Pilavo rocks fall almost entirely within the tholeiitic field as opposed to those from Pululahua and Pichincha (Fig. 9b). MgO displays positive correlations with Fe_2O_3 and CaO and negative correlations with Na_2O and K_2O (Fig. 9c–f). In contrast to major elements, incompatible trace element concentrations display a wide range of variability (Rb = 12–45 ppm, Sr = 650–1350 ppm, Ba = 600–1800 ppm, Zr = 80–225 ppm, Th = 4–24 ppm, Pb = 6–14 ppm, U = 1–6 ppm, La = 10–70 ppm, Ce = 20–120 ppm) and are significantly higher than at Pichincha and Pululahua (Fig. 9g and h), whereas compatible elements (Ni = 4–14 ppm, Cr = 4–19 ppm) are significantly lower (Fig. 9i and j). Incompatible elements are strongly correlated with each other (Fig. 9k).

In primitive mantle-normalized trace element diagrams (Fig. 8a), Pilavo rocks display typical subduction-related geochemical signatures with LILE enrichment and strong negative Nb and Ta anomalies. Compared with Pululahua and Pichincha, they show deeper P and Ti negative anomalies (Fig. 8a), a smaller negative Th anomaly and a general

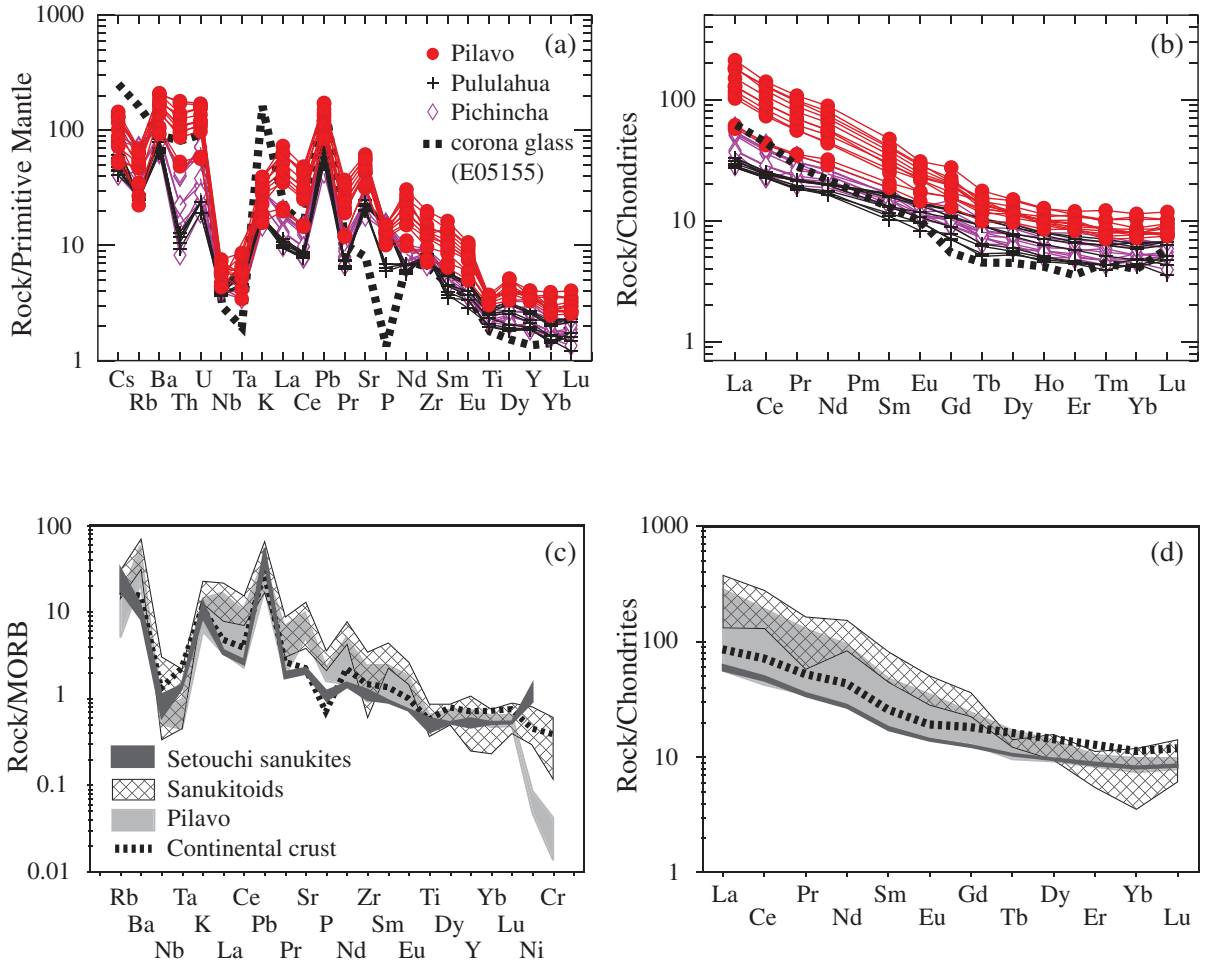

Fig. 8. (a) Primitive mantle-normalized trace element variation diagrams for the Pilavo rocks and of the corona texture glass around quartz xenocrysts (sample E05155) compared with those of Pichincha and Pululahua. The corona texture glass is the average of 12 LA-ICP-MS spot measurements. Normalizing values are from Sun & McDonough (1989). (b) Chondrite-normalized REE patterns of the Pilavo lavas and of the corona texture glass around quartz xenocrysts (sample E05155) compared with those of Pichincha and Pululahua. The corona texture glass is the average of 12 LA-ICP-MS spot measurements. Normalizing values are from Sun & McDonough (1989). (c) MORB-normalized trace element patterns of the Pilavo lavas compared with those of the average continental crust (Rudnick & Gao, 2004), Setouchi sanukites (Shimoda *et al.*, 1998; Tatsumi *et al.*, 2003), and sanukitoids (Martin *et al.*, 2005). The fields of Setouchi sanukites and sanukitoids represent ±1 standard deviations around the averages of element concentrations. It should be noted that compared with (a) some elements have been removed because they are not available in the sanukitoid and sanukite databases and Cr and Ni have been added. MORB-normalizing values are from Kelemen *et al.* (2004). (d) Chondrite-normalized REE patterns of the Pilavo rocks and of the corona texture glass around quartz xenocrysts (sample E05155) compared with those of the average continental crust (Rudnick & Gao, 2004), Setouchi sanukites (Shimoda *et al.*, 1998; Tatsumi *et al.*, 2003), and sanukitoids (Martin *et al.*, 2005). The fields of Setouchi sanukites and sanukitoids represent ±1 standard deviations around the averages of element concentrations. Compared with (c) Pr and Ho have been removed because they are not available in the sanukitoid database (see Martin *et al.*, 2005). Normalizing values are from Sun & McDonough (1989).

enrichment in all incompatible elements. In a mid-ocean ridge basalt (MORB)-normalized diagram including compatible elements (Fig. 8c) Pilavo lavas display some affinities with high-MgO andesites such as Setouchi sanukites (and average continental crust), from which they differ markedly in having higher Sr and P and significantly lower Cr and Ni contents. Pilavo rocks, especially the most enriched ones, display a remarkable affinity with Archean sanukitoids, from which they differ only in terms of their lower Ni and Cr contents (Fig. 8c). REE patterns are characterized by a moderately steep LREE to middle REE (MREE) slope, a flat MREE to HREE slope and the absence of negative Eu anomalies (Fig. 8b), and, except for the two least evolved rocks, are shifted to higher concentrations (especially LREE) compared with Pululahua and Pichincha. In the context of their REE patterns the Pilavo rocks show significant affinity both with Archean sanukitoids (the most enriched rocks) and with Setouchi sanukites (the least enriched rocks) (Fig. 8d). The affinity with Setouchi sanukites and Archean

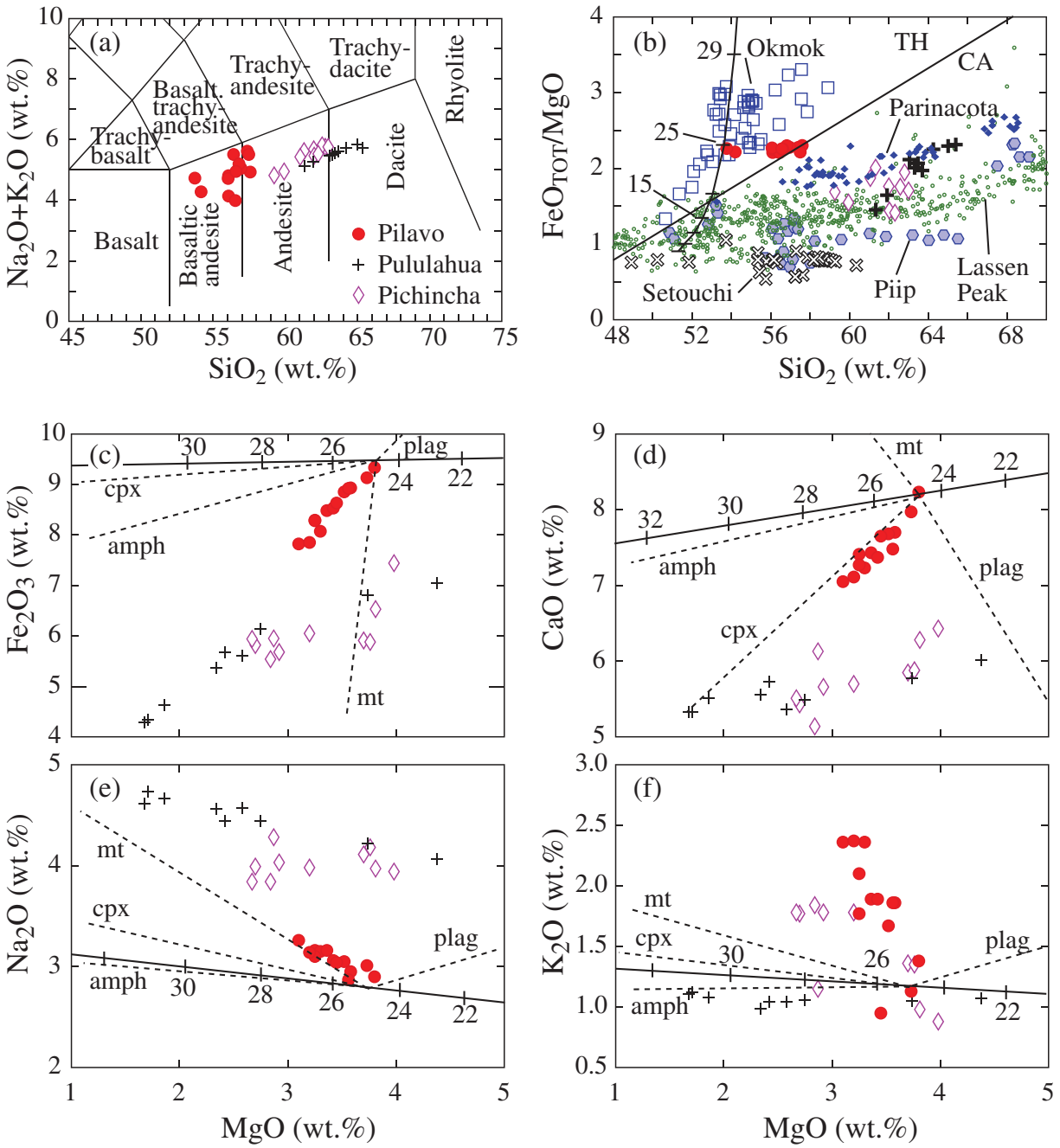

Fig. 9. (a) Total alkalis–silica diagram (Le Bas *et al.*, 1986) for Pilavo lavas compared with Pichincha and Pululahua. (b) $FeO_{tot}/MgO–SiO_2$ diagram (Miyashiro, 1974) for Pilavo lavas compared with other arc volcanoes (TH, tholeiitic; CA, calc-alkaline). Sources of data: Piip, Yogodzinski *et al.* (1994); Okmok, Finney *et al.* (2008); Lassen Peak, Clynne *et al.* (2008); Parinacota, Hora *et al.* (2009); Pululahua and Pichincha, Chiaradia *et al.* (2009). (c–j) MgO versus selected major and trace elements for Pilavo lavas compared with Pululahua and Pichincha. Modeled fractional crystallization trends of an average continental arc basalt (Kelemen *et al.*, 2004) fractionating 33% olivine, 64% clinopyroxene, and accessory amounts of Cr-rich spinel (~1%) and magnetite (~2%) are indicated by continuous lines. Tick marks and corresponding numbers represent the crystallized fraction (see Tables 4–6 for further details). Modeled fractional crystallization trends for amphibole, clinopyroxene, magnetite and plagioclase starting from the composition of a melt corresponding to 25% fractionation of the continental arc basalt according to the above model are indicated by the dashed lines (see Tables 4–6 for further details). (k) Modeling of repeated recharge and assimilation–fractional crystallization (AFC) processes in Ba–La space (see Table 7 for details). (l) Sr/Y vs K_2O for Pilavo lavas.

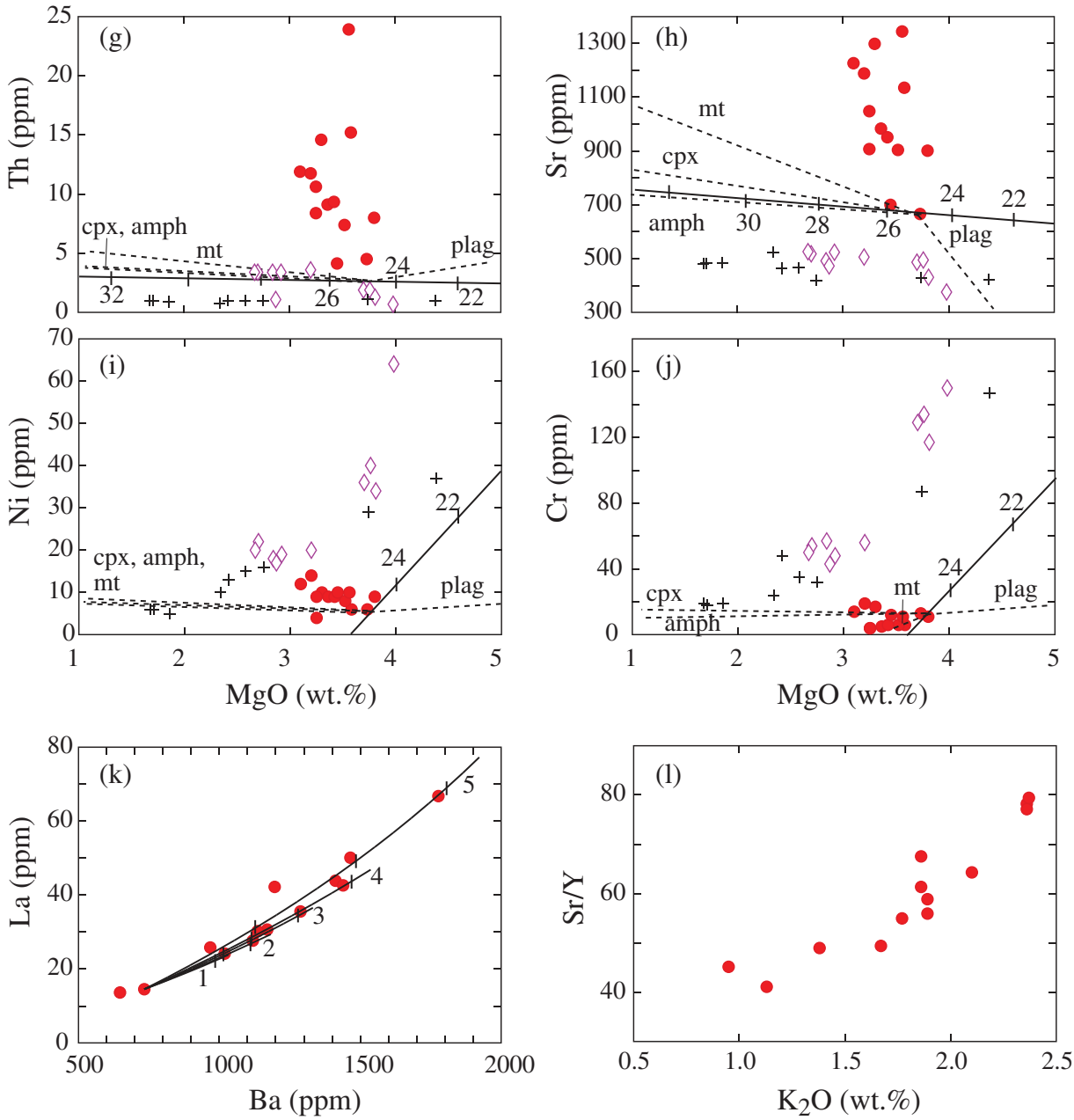

Fig. 9. Continued.

sanukitoids extends also to major elements (Table 3), with the exception of Fe_2O_3 (higher at Pilavo) and MgO (lower at Pilavo, but only with respect to Setouchi sanukites).

Some of the Pilavo rocks can be classified as adakite-like in terms of their Sr/Y (40–80) and La/Yb (10–40) values, but compared with Pichincha and Pululahua they have higher concentrations of Y (15–20 ppm) and Yb (1·2–2·0 ppm), which, for some samples, are beyond the threshold of adakites (Y ≤18 ppm; Yb ≤1·8 ppm; Martin *et al.*, 2005). Adakitic indices (e.g. Sr/Y, but also La/Yb and Dy/Yb), increase regularly with the degree of differentiation (e.g. K_2O; Fig. 9l).

Sr, Nd and Pb isotopes

The Sr, Nd and Pb isotopic compositions of the Pilavo rocks (Table 2) show little variability ($^{87}Sr/^{86}Sr = 0{\cdot}70377$–$0{\cdot}70390$, $^{143}Nd/^{144}Nd = 0{\cdot}51292$–$0{\cdot}51295$, $\varepsilon_{Nd} = +5{\cdot}5$ to $+6{\cdot}1$, $^{206}Pb/^{204}Pb = 19{\cdot}02$–$19{\cdot}08$, $^{207}Pb/^{204}Pb = 15{\cdot}57$–$15{\cdot}62$, $^{208}Pb/^{204}Pb = 38{\cdot}63$–$38{\cdot}85$) and are always more depleted

Table 3: Comparison of average major element compositions of Pilavo lavas, Archean sanukitoids and Setouchi sanukites

	SiO_2	TiO_2	Al_2O_3	Fe_2O_3	MgO	CaO	Na_2O	K_2O	P_2O_5	FeO/MgO
Sanukitoid average										
($n=31$)	58·76	0·74	15·8	5·87	3·9	5·57	4·42	2·78	0·39	1·35
1σ	2·90	0·30	0·90	1·50	1·30	1·50	0·70	0·80	0·10	0·42
Setouchi sanukite										
average ($n=30$)	57·38	0·6	15·87	6·23	7·22	6·59	3·15	1·74	0·15	0·78
1σ	1·85	0·11	0·78	0·7	1·34	0·54	0·39	0·36	0·02	0·22
Pilavo average										
($n=13$)	56·29	0·75	17·22	8·55	3·42	7·51	3·07	1·81	0·28	2·25
1σ	1·16	0·04	0·46	0·48	0·21	0·34	0·11	0·45	0·03	0·08
Residual difference										
Pilavo – sanukitoids (%)	=	=	+0·3	+8·2	=	+1·3	−17·6	=	=	+17·8
Residual difference										
Pilavo – sanukite (%)	=	=	+0·6	+13·3	65·8	0·5	=	=	28·6	52·0

Residual differences (%) represent the minimum per cent difference between the averages taking into account the 1σ errors (= means that the averages overlap within 1σ) and are calculated with respect to Pilavo average value. Data for Archean sanukitoids are from Martin *et al*. (2005) and those for Setouchi sanukites are from Shimoda *et al*. (1998) and Tatsumi *et al*. (2003).

with respect to Sr and Nd but more radiogenic for Pb than rocks of companion frontal volcanoes (i.e. Pululahua and Pichincha; Fig. 10). In both Sr–Nd (Fig. 10a) and Sr–Pb (Fig. 10b) isotope spaces the Pilavo compositions are slightly shifted towards the Galapagos Islands field compared with those of companion frontal arc volcanoes, but, like the latter, plot fully within the field of granulites and amphibolites of the Western Cordillera of Ecuador, which represent the metamorphic equivalents of the oceanic plateau rocks accreted to the continent in the Late Cretaceous (Amórtegui *et al.*, 2005; Chiaradia *et al.*, 2009). The Sr and Nd isotopic compositions of the microdrilled amphibole phenocryst and groundmass of sample E05156 are identical within error and are also similar to the whole-rock composition (Table 2).

Despite being characterized by a small range of isotopic variability the Pilavo lavas show significant correlations of Sr and Nd (not Pb) isotopes with incompatible elements and their ratios (Fig. 11). In general, $^{87}Sr/^{86}Sr$ values increase whereas $^{143}Nd/^{144}Nd$ values decrease with increasing incompatible element concentrations and their ratios (Fig. 11).

DISCUSSION

The main focus of this study is the petrogenesis of the Pilavo basaltic andesites and, in particular, the processes responsible for their enrichment in incompatible elements. Below, we discuss the steps, from magma source to magma differentiation at various crustal levels, at which such enrichment might have occurred. Finally, we discuss the tholeiitic affinity and the incompatible element enrichment of Pilavo basaltic andesites in a more general context.

Mantle source processes

In agreement with the geodynamic setting of the volcano, the available geochemical data indicate that Pilavo magmas are subduction-related (strong negative Nb and Ta anomalies; LILE enrichment). Therefore, following established models (e.g. Tatsumi, 1989) and in the absence of primitive magmatic rocks, the most reasonable parent magma of the Pilavo basaltic andesites is a hydrous basalt derived from partial melting of the mantle wedge metasomatized by a slab component. The most primitive samples from Pilavo have Ba/La (~50) and Pb/Ce (0·25–0·30), ratios similar to those of the most primitive magmas of the adjacent frontal arc volcanoes in Ecuador (Pululahua and Pichincha; Fig. 12a), indicating that the aqueous(?) (Ba and Pb are aqueous fluid-mobile elements; e.g. Kessel *et al.*, 2005) slab component contribution was probably similar for all three volcanoes. None the less, the more primitive isotopic compositions and significant enrichment in aqueous fluid-immobile incompatible elements (e.g. Th, La, Zr, Nb) as well as their ratios (e.g. Th/La, Th/Nb) in the Pilavo lavas, compared with those of Pichincha and Pululahua (Fig. 12b and c), might suggest a fundamental difference in the slab component or in the mantle source. High Th/La values (0·28–0·36) and Th concentrations (4–24 ppm), like those of the Pilavo andesites, are usually considered to reflect a subducted sediment (melt) component

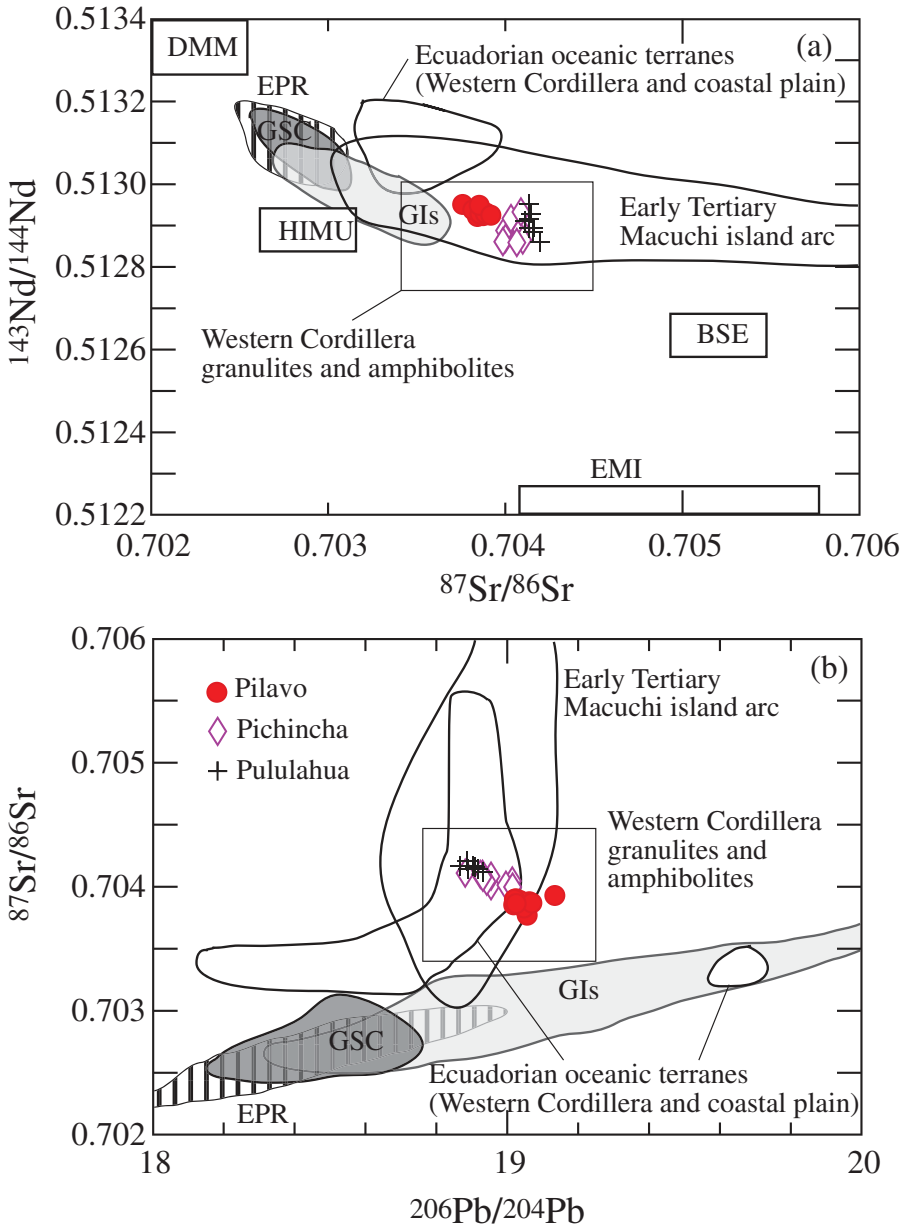

Fig. 10. Nd–Sr (a) and Sr–Pb (b) isotope variation in the lavas of the studied volcanoes in comparison with fields of various potential source reservoirs and rocks (data from Zindler & Hart, 1986; White *et al.*, 1993; Litherland *et al.*, 1994; Mamberti *et al.*, 2003; Amórtegui *et al.*, 2005; M. Chiaradia, unpublished data). DMM, Depleted MORB Mantle; EPR, East Pacific Rise; GSC, Galapagos Spreading Center; HIMU, high μ; GIs, Galapagos Islands; BSE, Bulk Silicate Earth; EMI, Enriched Mantle I.

in the mantle source (e.g. Plank, 2005) and therefore might suggest a higher subducted sediment melt contribution at Pilavo than at Pichincha and Pululahua. However, the high Th/La values and Th concentrations of Pilavo lavas are inconsistent with their isotopic signatures, which are more depleted than those of Pululahua and Pichincha (Figs 10a, b and 12c). Furthermore, subducting sediments at adjacent trench locations (Colombia and Peru, Plank & Langmuir, 1998; no geochemical data are available for sediments of the Ecuadorian trench to our knowledge) and Carnegie Ridge lavas (Harpp *et al.*, 2005) have low Th/La values (0·021–0·15 and 0·034–0·092, respectively), implying that the high Th/La values of the Pilavo rocks are not the result of sediment and/or oceanic crust melting and might, instead, be the result of intracrustal magmatic processes (see also Plank, 2005). This, however, does not exclude the possibility that the metasomatizing agent responsible for mantle wedge flux melting in the subduction zone beneath Pilavo may be a hydrous melt, as suggested for subduction zones in general by thermal modeling of

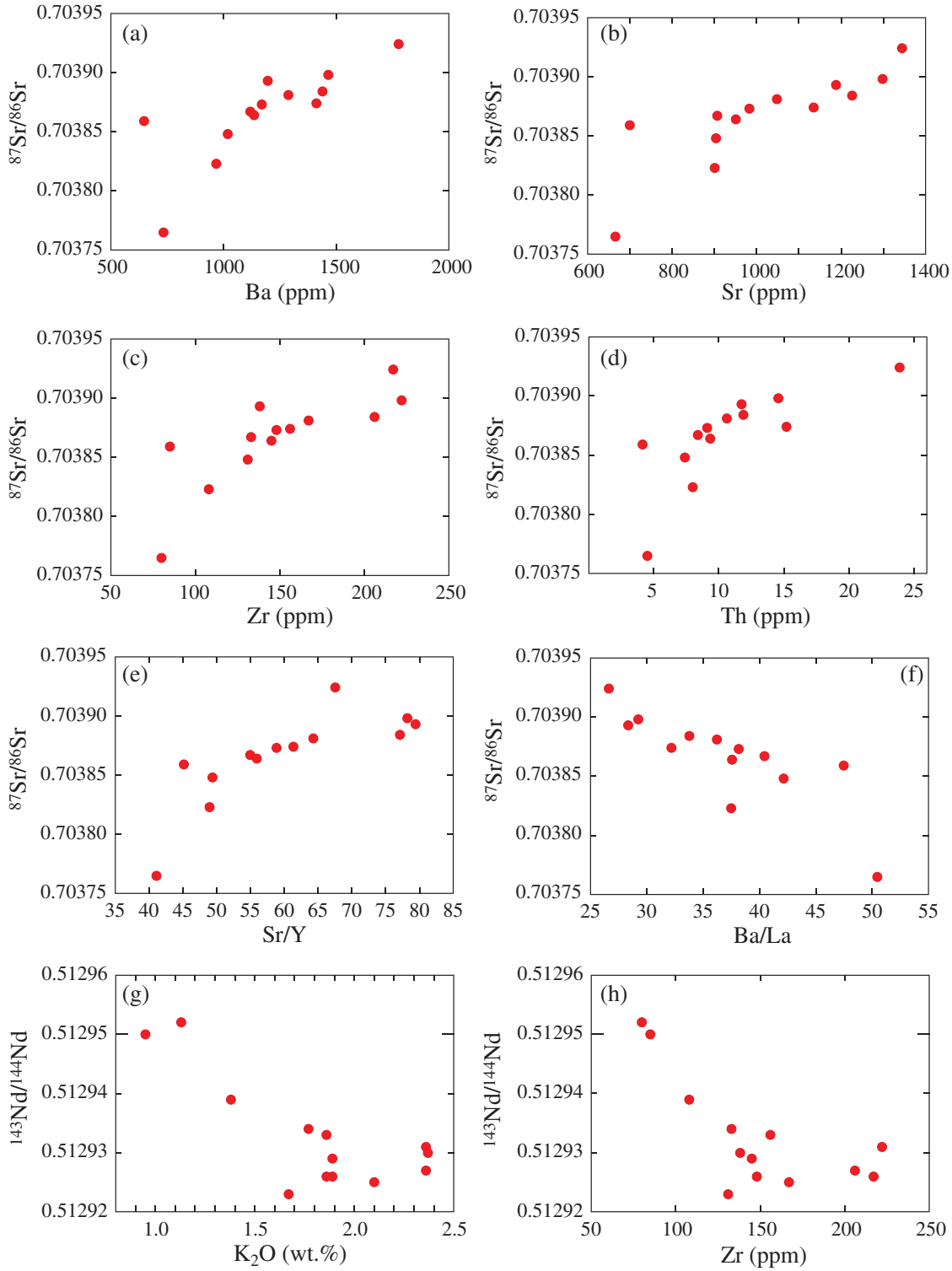

Fig. 11. Correlations between whole-rock radiogenic isotope compositions and various incompatible trace elements and ratios (for discussion see text).

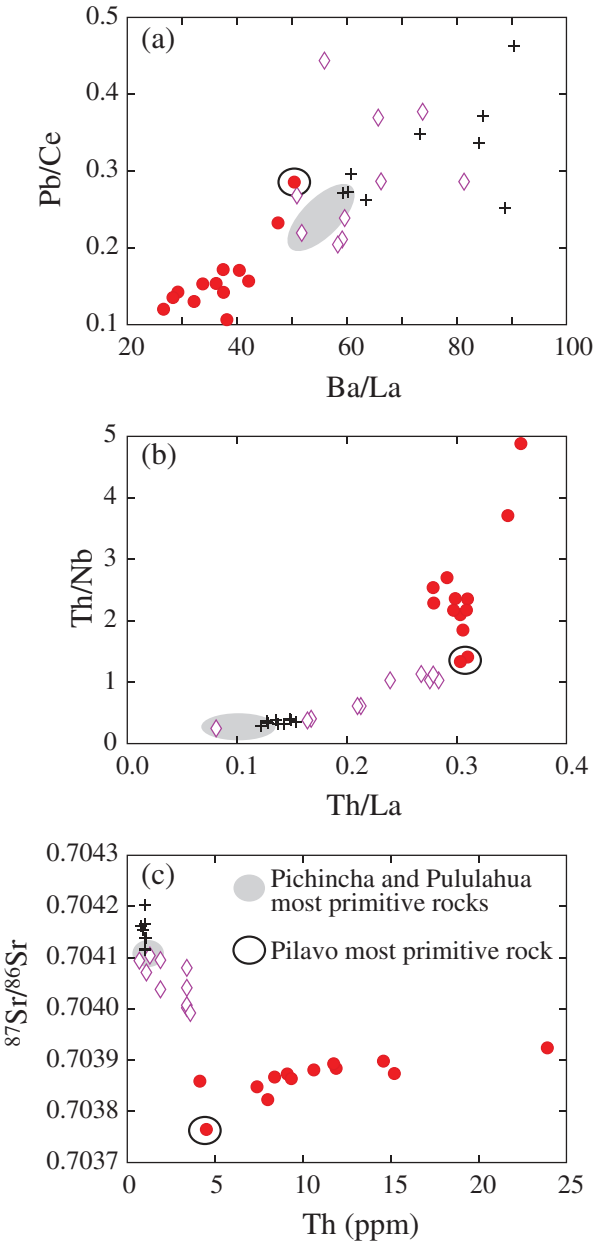

Fig. 12. Pb/Ce vs Ba/La (a), Th/Nb vs Th/La (b) and $^{87}Sr/^{86}Sr$ vs Th (c) plots for Pilavo, Pululahua and Pichincha volcanoes (for discussion see text).

subducted slabs (van Keken *et al.*, 2002; Kincaid & Griffiths, 2004; Plank *et al.*, 2009), experimental studies on element partitioning (e.g. Kessel *et al.*, 2005), and trace element data on high-pressure rocks (Hermann *et al.*, 2006).

High-pressure olivine and clinopyroxene fractionation

The very low compatible element concentrations at low SiO_2 contents (e.g. Ni = 6–14 ppm, Cr = 4–19 ppm, Mg-number ~0·44–0·45) even of the least evolved (i.e. MgO-, Fe_2O_3-, CaO-richer) Pilavo rocks, which are much lower than the andesitic–dacitic companion frontal volcanoes situated more to the south (Fig. 9), suggest extensive fractional crystallization of olivine and clinopyroxene. High Al_2O_3 (~18 wt %) and Sr (~700 ppm) contents in the most primitive basaltic andesites of Pilavo indicate the lack of significant plagioclase fractionation. A liquidus assemblage of olivine and clinopyroxene (without plagioclase), resulting in depletion of MgO and Ni and enrichment of Al_2O_3 but no significant enrichment of SiO_2, is typical of high-pressure (e.g. mantle–crust interface) fractionation of mantle-derived basaltic melts and generates high-Al_2O_3 hydrous basalts and basaltic andesites (see also Crawford *et al.*, 1987; Foden & Green, 1992; Müntener *et al.*, 2001). We have modeled fractional crystallization of a primitive magma with the composition of an average continental arc basalt (Kelemen *et al.*, 2004), involving a clinopyroxene- and olivine-dominated high-pressure assemblage (continuous black lines in Fig. 9). Modeling can reproduce consistently the major and trace element geochemistry of the least evolved rocks of Pilavo for ~25% fractional crystallization of a bulk assemblage consisting of olivine (~33%), clinopyroxene (~64%), plus accessory amounts of magnetite (2%) and magnesiochromite (1%) (see Tables 4–6 for further details). Although based on a primitive melt composition that does not necessarily correspond to that of the Pilavo parental magmas and on proportions of the fractionating assemblage that cannot be verified, this modeling exercise shows that, as a first approximation, high-pressure fractionation of spinel-bearing olivine-clinopyroxenite from a primitive arc basalt is a suitable process to explain the strong compatible element depletion of the Pilavo basaltic andesites. Importantly, our modeling also shows that such a fractionating assemblage will drive the primitive basaltic melt into the tholeiitic field (Fig. 9b), reproducing the tholeiitic compositions of the least evolved Pilavo rocks for ~25% crystallization, consistent with our modeling of the other major and trace elements (Fig. 9c–j). However, if the least evolved rocks of Pilavo can be derived by high-pressure olivine-clinopyroxenite fractionation of a primitive arc basalt, the geochemical trends of the Pilavo rocks (Fig. 9b–j) require in contrast either a different fractionating assemblage or alternative magmatic processes.

Recharge and mixing in crustal magma chamber(s)

Clinopyroxene, amphibole, plagioclase and magnetite are the dominant phenocryst phases in the Pilavo basaltic andesites as well as in the Pululahua and Pichincha andesites or dacites. Figure 9 shows model fractionation trends resulting from the removal of each of these mineral phases. The variations in major and trace element concentrations of Pululahua lavas (notably K_2O, Th and Sr: Fig. 9f, i and j) can be explained almost entirely by

Table 4: Compositions of primitive melts used for the modeling curves reported in Figure 9

Primitive melt*	Model	SiO_2	TiO_2	Al_2O_3	FeO_{tot}	MnO	MgO	CaO	Na_2O	K_2O	P_2O_5	Cr	Ni	Th	Sr	Total	Ref.
Continental arc	1	51·33	0·98	15·7	8·72	0·17	9·48	9·93	2·61	0·88	0·22	398	159	2·03	426	100·10	1
E05065	2	56·07	0·71	17·85	8·22	0·16	3·73	7·97	3·01	1·13	0·23	13	6	4·5	666	99·08	2

*Oxides in wt %, trace elements in ppm.
Model 1 refers to the modeling of the high-pressure stage at the mantle–crust interface or within the lower crust. Model 2 refers to the modeling of the Pilavo series rocks at mid-crustal levels (see text for further details). References: 1, Kelemen *et al*. (2004); 2, this study. Because Kelemen *et al*. (2004) provided an average composition from $n = 427$ analyses without standard deviations we have allowed a variability of ±0·5 wt % for CaO and Na_2O and of ±75 ppm for Sr in our model (for which the average continental arc composition would be too high in CaO and Na_2O and too low in Sr to reproduce the primitive composition of sample E05065 for these elements). The allowed uncertainties are within the natural variability of arc basalts.

Table 5: Compositions of mineral phases

Mineral	Sample	SiO_2	TiO_2	Al_2O_3	Cr_2O_3	FeO_{tot}	MnO	MgO	CaO	Na_2O	NiO	K_2O	Total	Ref.
Model 1														
cpx	Run 10	49·35	0·34	7·49	0·03	5·65	0·16	15·57	21·24	0·32		0·01	100·16	1
olivine	E05024-8		39·59	0·03	0·05	11·11	0·24	48·64	0·08	0·01		0·27	100·01	2
spinel	Run 10	0	0·3	42·13	13·85	24·83	0	14·08	0·21	0·03	0·13	0	95·56	1
Magnetite	E05151__1__2	0·07	5·58	3·49	0·02	77·79			0·50		7·79	0·03	95·27	3
Model 2														
cpx	E156a__6-2	49·71	0·590	4·690	0·050	9·75	0·430	13·38	20·89	0·460	0·010	0·020	99·98	3
amphibole	E05067__2__1	41·66	1·74	12·70	0·01	13·09	0·12	13·44	11·27	2·00	0·02	1·26	97·31	3
magnetite	E05151__1__2	0·07	5·58	3·49	0·02	77·79			0·50		7·79	0·03	95·27	3
plagioclase	E05067	47·09	0·01		33·15		0·64	0·05	16·43		1·78	0·09	100·01	3

References: 1, Kägi (2001), mineral compositions are from experimental runs on calc-alkaline basalt at 1 GPa and 1170–1200°C; 2, unpublished data (M. Chiaradia) from olivine of a basaltic andesite of Chacana (Eastern Cordillera of Ecuador); 3, this study.

Table 6: Proportions of fractionating minerals in Model 1

	Olivine	Clinopyroxene	Magnesiochromite	Magnetite
wt %	33	63·6	1·4	2

fractionation of a clinopyroxene–amphibole–magnetite ± plagioclase assemblage, consistent with the minimal isotopic variations observed at this volcano (Chiaradia *et al.*, 2009). At Pichincha, fractionation processes cannot entirely explain the Th and especially the K_2O enrichment: assimilation of crustal material is required, in agreement with the correlations observed between radiogenic isotopes and fractionation indices at this volcano (Chiaradia *et al.*, 2009). At Pilavo fractionation of variable proportions of clinopyroxene, amphibole–magnetite ± plagioclase could explain the variations in Fe_2O_3, CaO, Na_2O (Figs 9c–e), and possibly Cr and Ni with MgO (Figs i–j), but clearly cannot explain the strong enrichments in K_2O, Th, Sr (Figs 9f, g–h) and all other incompatible elements (not shown). This is consistent with the petrography, mineral chemistry and correlations of Sr and Nd isotopes with incompatible elements, which indicate that the Pilavo magmas have evolved in an open crustal magma storage system through either combined assimilation–fractional crystallization (AFC) or recharge accompanied by assimilation–fractional crystallization (RAFC).

A simple AFC process is incompatible with petrographic evidence of magma mixing such as the occurrence of mingling textures, of texturally different phenocrysts within the same sample, and of magmatic quartz xenocrysts

(see above). A dynamic process of RAFC (e.g. Bohrson & Spera, 2003) with continuous homogenization of the evolving magmas, their partial solidification to form unconsolidated crystal mushes or proto-plutons and their assimilation by recharges of more mafic magma is more appropriate for the petrogenesis of the Pilavo lavas, as indicated by the systematically changing petrographic, geochemical and isotopic compositions of whole-rocks and minerals.

Petrographic evidence for magma mixing (or mush or proto-pluton incorporation) in the Pilavo lavas is provided by the coexistence of texturally and compositionally different pheno- or xenocrysts in the same thin section: (1) unzoned to normally zoned Mg-rich amphibole phenocrysts and inversely multi-zoned large amphibole; (2) amphiboles with or without equant clinopyroxene coronas, perhaps indicative of heating (Rutherford & Devine, 2003); (3) clinopyroxene associated with amphibole in clots (perhaps residues of magma mushes), as isolated large phenocrysts with sector zoning (probably crystallized rapidly near the surface; Brophy *et al.*, 1999) or surrounded by amphibole coronas (relic clinopyroxenes); (4) plagioclases with heavily sieved, slightly sieved, and non-sieved cores. Additional evidence of magma mixing or mush incorporation comes from plagioclase compositions. Variably sieved to non-sieved cores of plagioclase phenocrysts display high anorthite contents ($An_{80–92}$) indicating crystallization from H_2O-rich magmas and/or from melts with high CaO/Na_2O ratios and Al_2O_3 contents (e.g. Sisson & Grove, 1993; Panjasawatwong *et al.*, 1995). Feig *et al.* (2006) have shown experimentally that plagioclase with anorthite contents between 80 and 85 mol % can crystallize only for water contents of about 5 wt % at $P = 0{\cdot}2$ GPa. Anorthite-rich cores of plagioclase phenocrysts in the Pilavo rocks have both low and high Sr contents: the least evolved rocks contain only plagioclase with Sr-poor cores, whereas progressively more evolved rocks contain plagioclase with both Sr-poor and increasingly Sr-rich cores (compare analyses pl67.3-1, pl67.3-8 and pl67.7-2 in Electronic Appendix 3). Because Sr contents in plagioclase decrease with increasing anorthite content (Blundy & Wood, 1991) and increase with Sr concentration in the melt, the occurrence of two types of similarly anorthite-rich plagioclase with different Sr contents in the more evolved rocks indicates mixing of these plagioclases during or after their crystallization from melts with different Sr contents.

Evidence for recharge of felsic magmas, crystal mushes or unconsolidated proto-plutons by more mafic magmas comes from the presence of quartz xenocrysts only in the more evolved rocks. Also, following previous interpretations (e.g. Sato, 1975; Stimac & Pearce, 1992; Mashima, 2004), these are most probably phenocrysts of a felsic magma (or mush or unconsolidated proto-pluton), which have produced the typical zoned corona textures with glass around the quartz xenocryst and clinopyroxene on the outer part through reaction with the recharging mafic magma. It is unlikely that they represent xenocrysts derived from mature continental crust because the Western Cordillera of Ecuador is floored by mafic oceanic plateau crust (e.g. Feininger & Seguin, 1983; Vallejo *et al.*, 2006, 2009; Chiaradia, 2009) and assimilation of a quartz-rich mature continental crust should result in a significant shift of radiogenic isotope compositions, which are instead primitive for all rocks (see above).

Amphibole and clinopyroxene phenocrysts in the Pilavo lavas display systematic correlations in their incompatible element contents with whole-rock chemistry (Figs 4–6). The intra-sample variability (e.g. standard deviation) of these elements is similar for all samples and somewhat less than the inter-sample variability. Because each sample investigated represents a different lava flow (Fig. 2b), this suggests that amphiboles and clinopyroxenes have crystallized from differently evolved and relatively (though not completely) homogenized magmas, before being erupted. The identical Sr and Nd isotopic compositions of a large zoned amphibole phenocryst and the surrounding groundmass (sample E05156) support such a conclusion.

Whole-rock incompatible element contents (e.g. Sr) correlate with modal mineralogy (Fig. 13a, c and e). In particular, they increase with increasing modal amphibole (Fig. 13c) and (in a semi-quantitative way; see above) with the proportion of quartz xenocrysts. Because in the more evolved Pilavo rocks a portion of the amphibole population consists of multiply zoned amphibole crystals (see above), which reflect growth episodes under different magmatic conditions and thus probably represent xenocrysts, and because quartz crystals are magmatic xenocrysts, we suggest that the incompatible element enrichment was concomitant with a steadily growing incorporation of evolving magmas, crystal mushes or proto-plutons.

In agreement with the above observations, geochemical modeling (Fig. 9k) shows that the enrichment of incompatible elements of Pilavo rocks can be successfully reproduced by a process in which the same primitive magma (most primitive rock of the Pilavo series) recharges, fractionates, and assimilates a few times increasingly evolved magmas, mushes or proto-plutons (represented by samples of the Pilavo series). The modeling implies a high r value of 0·9 (r = mass of assimilant/mass of crystallized magma), which is typical for a thermally mature assimilant, such as crystal mush, unconsolidated proto-pluton or crystal-rich magma in the case of Pilavo. For each RAFC step the resulting amounts of fractionation and assimilation are low (5–12% fractionation and 4·5–11% assimilation; Fig. 9k, Table 7) and thus consistent with the small variability of major elements for a concomitant strong enrichment in incompatible elements.

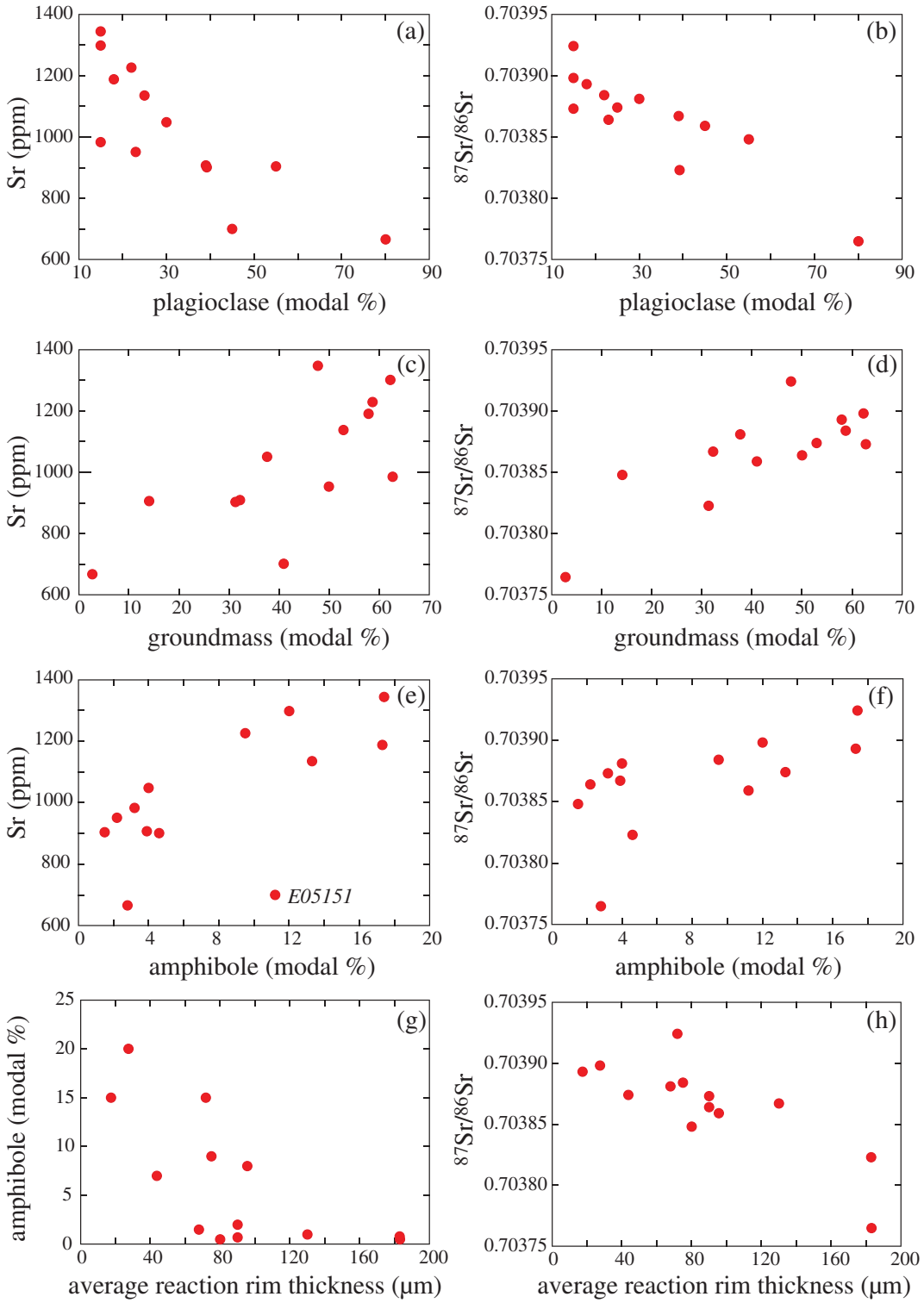

Fig. 13. (a–f) Correlations between modal mineralogy and geochemical and isotopic composition of the whole-rocks. A noteworthy feature is the high amphibole modal content (11%) in sample E05151, which is 'anomalous' for being characterized by a low Sr content (700 ppm) but a radiogenic Sr isotope signature (0·703859). (g, h) Correlations between the average thickness of reaction rims around amphibole and corresponding Sr isotopic composition and amphibole modal abundance of the whole-rocks.

Table 7: Parameters used for modelling repeated recharge and assimilation–fractional crystallization processes at Pilavo (refer to Fig. 9k)

Step	D_{Ba}	D_{La}	Tick marks of *F* in Fig. 9	Fractionation (wt %)	Assimilation (wt %)	Scheme of recharge
1	0·3	0	0·05	5	4·5	E05065 → E05065 to yield E05148
2	0·3	0	0·05	5	3·6	E05065 → E05148 to yield E05064
3	0·35	0	0·035	7	6·3	E05065 → E05064 to yield E05154
4	0·35	0	0·04	8	7·2	E05065 → E05154 to yield E05149
5	0·45	0	0·04	12	10·8	E05065 → E05149 to yield E05152

Compositions of samples used for modelling are reported in Table 2.

Crustal assimilation and melting

Petrographic and geochemical evidence that plagioclase crystallization postdates that of amphibole in the Pilavo basaltic andesites suggests magmatic evolution at relatively high pressures (≥0·4 GPa). Experimental studies have shown that in H_2O-rich oxidized basaltic systems amphibole crystallization precedes plagioclase at pressures ≥ ~0·4 GPa (e.g. Grove *et al.*, 2003; Feig *et al.*, 2006). Petrographic evidence of late plagioclase crystallization derives from the fact that the great majority of the plagioclase occurs as microcrysts and microlites in the groundmass. Late crystallization of plagioclase (largely post-amphibole and post-clinopyroxene) is also supported by steadily increasing Sr contents (and Sr/Y ratios) with magma evolution not only in whole-rocks but also in amphibole and clinopyroxene phenocrysts of all lava samples (Figs 4c and 5 b).

Assimilation and eventually melting of the crust at such mid-crustal levels is favored by a high rate of mafic magma supply and by magmas residing at these levels for enough time to cause thermal maturation of the host rocks (e.g. Petford & Gallagher, 2001; Dufek & Bergantz, 2005; Annen *et al.*, 2006; Lee *et al.*, 2006). At Pilavo assimilation of crustal material by magmas that were undergoing the RAFC processes described in the previous section is supported by the systematic correlations of Sr and Nd isotopes with magma differentiation indices (Fig. 11) and mineral modal abundances (Fig. 13b, d and f). The basement in this part of the Western Cordillera of Ecuador is represented by a Cretaceous oceanic plateau, which at mid- to lower crustal levels may have been modified by arc magmas continuously moving through the crust since the Late Cretaceous–Early Tertiary (Chiaradia, 2009; Chiaradia *et al.*, 2009). Such long-lived refinement processes of the Cretaceous oceanic plateau by arc-related magmas might have created a hybrid crust with an isotopic composition close to that of the Quaternary arc magmas (see Fig. 10 and Chiaradia *et al.*, 2009) and thus consistent with the small isotopic shifts observed within the Pilavo series. Partial melting of mafic mid- to lower crustal amphibole-bearing lithologies (e.g. Davidson *et al.*, 2007) can produce K-rich granitic melts (Sisson *et al.*, 2005) and such melts could also be enriched in incompatible elements. Experimental work by Storkey *et al.* (2005) has shown that incompatible element concentrations in partial melts of lower crustal metabasites are several hundred to several thousand times higher than primitive mantle concentrations. Partial melting of tonalite at mid-crustal levels also produces high-K dacitic melts that are likely to be enriched in incompatible elements (e.g. Singh & Johannes, 1996; Reubi & Blundy, 2008). In concomitance with the RAFC processes described above, incorporation of these enriched partial melts into crystal mushes and proto-plutons recycled by recharging magmas might be an additional process to explain the strong and steady enrichment of incompatible elements in concomitance with subtle radiogenic isotope changes in the Pilavo magmas (Fig. 11).

Mixing in the conduit during magma ascent

Analysis of amphibole reaction rim thickness provides evidence that further mixing occurred, at least in the more primitive rocks, in magmatic conduits at pressures below those of amphibole stability. Hydrous silicate minerals that have crystallized from an H_2O-rich magma at depth will become unstable as the solubility of H_2O in the decompressing silicate liquids decreases (e.g. Shaw, 1974). Destabilization through such a process results in the formation of reaction rims around amphibole crystals in contact with melt, consisting of an assemblage of pyroxene, plagioclase and Fe–Ti oxides (e.g. Rutherford & Hill, 1993). The onset of amphibole destabilization depends on the magma composition and temperature but typically occurs at

pressures below 150–100 MPa (e.g. Rutherford, 2008). The thickness of the reaction rims developed around amphibole phenocrysts, as well as the size and shape of the replacing mineral phases (plagioclase, pyroxene, Fe-oxides), depends on the magma ascent rate (e.g. Rutherford & Hill, 1993; Browne & Gardner, 2005). Thicker reaction rims indicate longer exposure times (slower ascent rates) at disequilibrium between amphibole and the surrounding melt and are usually accompanied by equant and larger sized replacing mineral phases (Browne & Gardner, 2005). In contrast, thinner rims with a smaller grain size of the replacing minerals and acicular shapes are typical of faster and continuous ascent rates (Browne & Gardner, 2005). Reaction rims around amphibole phenocrysts therefore provide qualitative information about the path of the magma between the depth of initial amphibole breakdown and the effusion at the vent.

We note that the average thickness of reaction rims on the amphibole population of each sample correlates broadly with amphibole geochemical indices (Fig. 5e and f) as well as with the modal amount of amphibole, whole-rock geochemical indices, and whole-rock $^{87}Sr/^{86}Sr$ values (Fig. 13g and h). Less evolved rocks are thus characterized by less abundant amphibole with low incompatible element contents (Fig. 13e and f) and variably thick reaction rims (Fig. 13h), whereas more evolved rocks contain more abundant amphibole enriched in incompatible elements and with consistently thinner rims. This suggests that the less evolved magmas ascended slowly and mixed with each other in the conduit at a pH_2O below that of amphibole stability to account for the coexistence of amphiboles with variably thick reaction rims in the same thin section, whereas more evolved magmas have ascended more rapidly from the magma storage chamber with no significant mixing in the conduit. This is qualitatively in line with the negative correlation of modal plagioclase with whole-rock geochemical differentiation (Fig. 13a and b). Because the vast majority of plagioclase in the Pilavo rocks consists of microcrysts (a likely result of decompression crystallization during slow ascent), the above correlation suggests that the highest amount of decompression crystallization occurred in the slowly ascending, least evolved magmas.

Oxygen fugacity of the magmas

Oxygen fugacities estimated from magnetite–-ilmenite pairs in the Pilavo lavas are high (from NNO +1·5 to NNO +3·3). However, Scaillet & Evans (1999), among others, have highlighted that fO_2 values >NNO +1·5 are outside the calibrated range of Fe–Ti-oxide barometry and, by measuring experimentally fO_2 for Pinatubo, they determined an fO_2 that is about 1 log unit below that established by Fe–Ti-oxide barometry. Assuming a similar correction for the Pilavo lavas, fO_2 values none the less remain high and vary between NNO + 0·5 and about NNO + 2.

The high fO_2 of the Pilavo lavas might indicate oxidizing conditions in the mantle source, although further oxidation may have occurred within the crust. In fact, in H_2O-rich magmas that are crystallizing amphibole, like those of Pilavo, fO_2 increases owing to liberation of free O_2 during amphibole crystallization (Frost & Lindsley, 1991). The inverse MgO zoning in the Pilavo amphiboles and associated opacitization of the rims at each subsequent growth zone would be consistent with increasing fO_2 during magmatic evolution (e.g. Mason, 1978).

General model

Mantle-derived basaltic magmas initially underwent high-pressure fractionation of dominant olivine and clinopyroxene with lesser amounts of Cr-rich spinel and magnetite at the mantle–crust interface and/or at lower crustal levels (Fig. 14). This fractionating assemblage drove derivative liquids into the tholeiitic field (Fig. 9b) and towards high H_2O and Al_2O_3 contents, and low Ni and Cr contents. These hydrous, high-Al_2O_3 basalt to basaltic andesite melts migrated upwards, where they evolved at mid-crustal levels through dominant amphibole and clinopyroxene ± plagioclase fractionation under high pH_2O.

Although no age determinations are available for the various lava flows investigated here, volcanic stratigraphy suggests that the more evolved and crustally contaminated lava flows belong to the later (main) phase of build-up of the volcanic edifice (Fig. 2b). From this point of view, the correlations between modal abundance of amphibole, mineral chemistry, radiogenic isotopes and geochemical indices of whole-rock differentiation point to the following model (Fig. 14). Initially (Stage a in Fig. 14) the high-Al_2O_3 basalt to basaltic andesite magmas ascended relatively rapidly, crystallizing little amphibole and allowing for abundant decompression crystallization of plagioclase and clinopyroxene only at shallow crustal levels (mostly outside the amphibole stability field) when magmas started to exsolve water and consequently to slow down until stalling in the conduit or in shallow magma chambers. At this stage a significant mid-crustal reservoir was not yet established, as indicated by the paucity of amphibole phenocrysts, the lack of zoned amphiboles and the homogeneously low Sr contents of plagioclase in these magmas. Mixing probably occurred in the conduit at depths shallower than those of amphibole stability between magmas stalled owing to the onset of abundant decompression crystallization and batches of magma rising from depth. This scenario is supported by the coexistence of amphiboles with variably thick reaction rims only in the early stage, more primitive rocks of Pilavo.

The subsequent establishment of one or several mid-crustal magma reservoirs (Stages b and c in Fig. 14), where magmas evolved through amphibole and

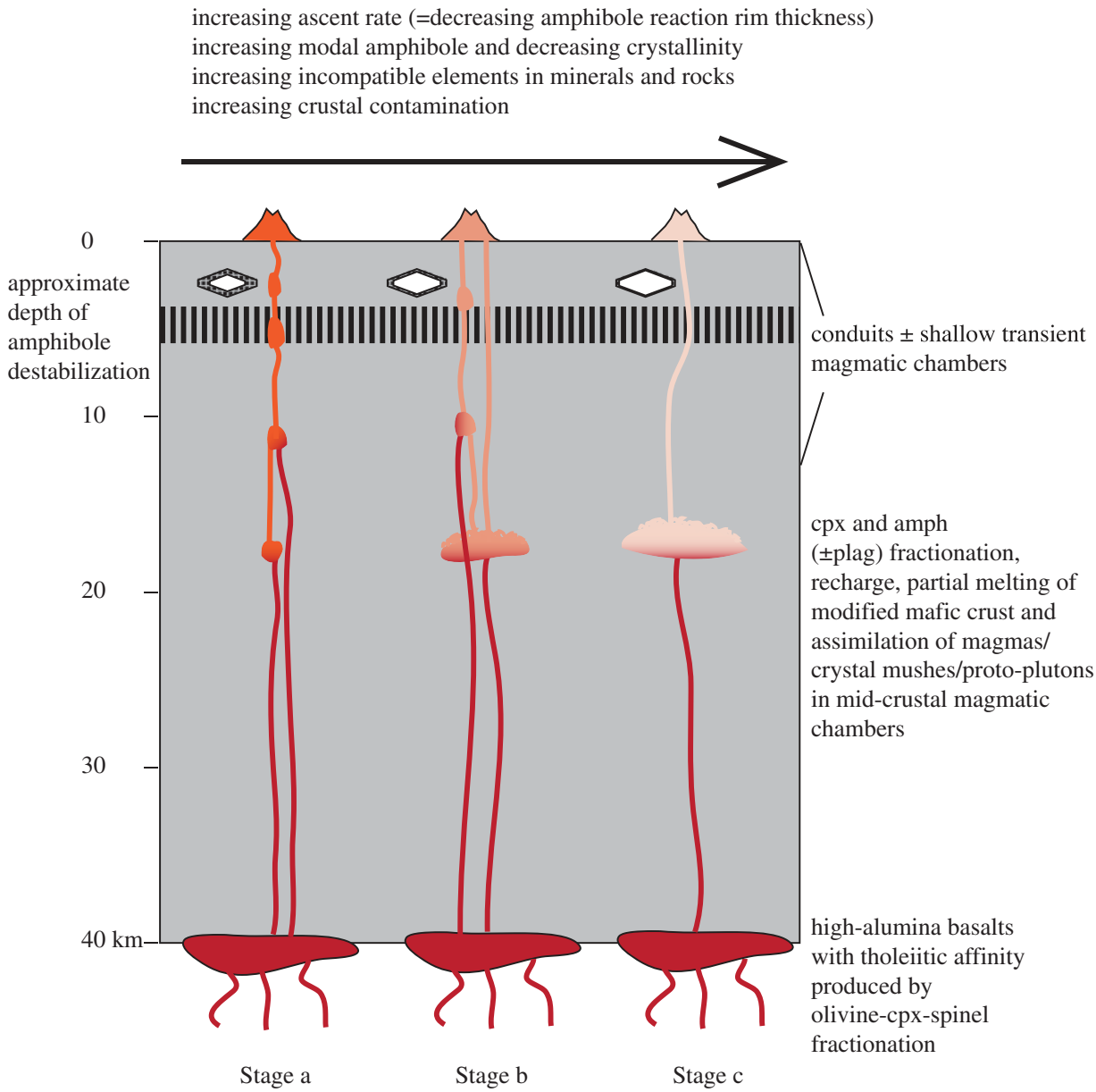

Fig. 14. Conceptual model of the magmatic plumbing system at Pilavo volcano, inspired by the deep hot zone model of Annen *et al.* (2006) (for discussion see text). Lighter colors indicate progressively enriched magmas. Stages a, b, c do not necessarily correspond to systematically younger stages of volcano evolution. At Pilavo, the volcanic stratigraphy seems to suggest that Stage b postdates Stage a, but there is no constraint on the temporal relationships between Stage b and Stage c. The model may also be valid for Stage a postdating Stage b as a result of a changing plumbing system in which magmas short-circuit (Stage a) or not (Stages b and c) the mid-crustal chamber(s).

clinopyroxene fractionation under high pH_2O conditions ($P \geq 0{\cdot}4$ GPa), accompanied by assimilation of felsic magmas, crystal mushes or proto-plutons as well as mixing with incoming batches of mafic magma (RAFC processes), is marked by the appearance of multiply zoned amphibole in lavas of the main volcanic stage, increasingly Sr-rich plagioclase (coexisting with Sr-poor plagioclase) and magmatic quartz xenocrysts. During these RAFC processes incompatible elements became strongly enriched in progressively evolving magmas, as indicated by their correlations with radiogenic isotopes (Fig. 11) and amphibole abundance (Fig. 13), and as supported by our modeling (Fig. 9k). Magmas were driven towards the calc-alkaline field as a result of such processes (Fig. 9b). Correlations of average amphibole reaction rim thickness with amphibole mineral chemistry, whole-rock geochemistry and isotopic compositions suggest that increasingly enriched magmas were amalgamated in the mid-crustal

reservoir and ascended to the surface with steadily faster ascent rates above the depths of amphibole stability, probably owing to their increasingly H_2O-rich nature. The above model is also valid for the case in which Stages a, b and c of Fig. 14 represent plumbing systems at different, but not sequential, times, in which magmas short-circuit (Stage a) or not (Stages b and c) the mid-crustal chamber(s) (see also Hora *et al.*, 2009).

CONCLUDING REMARKS

The main focus of this work has been to understand the formation processes of the enriched basaltic andesites of Pilavo. We have shown that Pilavo is distinct from adjacent frontal arc volcanoes in Ecuador in having a tholeiitic affinity and a strong enrichment in incompatible elements. Below we briefly discuss these features in a broader context through comparisons of Pilavo with other tholeiitic and andesitic arc volcanoes and with other types of enriched andesites (e.g. Setouchi sanukites and sanukitoids).

Tholeiitic vs calc-alkaline trends at Pilavo

Figure 9b shows Pilavo lavas plotted in a FeO_{tot}/MgO vs SiO_2 diagram (Miyashiro, 1974) together with various arc volcanoes displaying either tholeiitic or calc-alkaline affinity. The Pilavo lavas plot almost entirely within the tholeiitic field, although they do not define a typical tholeiitic trend such as that of Okmok volcano. Instead, they define a trend similar to those of calc-alkaline volcanoes (Pichincha, Pululahua, Lassen Peak, Piip, Setouchi) with an almost invariant FeO_{tot}/MgO for changing SiO_2. However, Pilavo is clearly distinct from the calc-alkaline volcanoes because its 'calc-alkaline trend' occurs at higher FeO_{tot}/MgO values (i.e. within the tholeiitic field). In detail, calc-alkaline volcanoes often define sub-horizontal trends at various FeO_{tot}/MgO values, with Parinacota being the closest to Pilavo. We concur with Hora *et al.* (2009) that, in an arc setting, such sub-horizontal trends at variably high FeO_{tot}/MgO ratios reflect magmas that have evolved at lower crustal levels with little further evolution at shallower levels for the tholeiitic end of the trend and magmas that underwent shallower level contamination and fractionation processes for the calc-alkaline end of the trend. If so, then the occurrence of sub-horizontal trends at variable FeO/MgO values would reflect different degrees of clinopyroxene- and olivine-dominated fractionation at deep levels, with Pilavo being an extreme case of olivine-clinopyroxenite fractionation.

Contrasting tholeiitic and calc-alkaline evolutionary trends in adjacent volcanoes such as Pilavo, Pichincha and Pululahua, are not uncommon in magmatic arcs (e.g. Singer & Myers, 1990). This has been attributed either to changes in the magmatic plumbing system of the volcano in time or space (e.g. Hora *et al.*, 2009), to spatial changes in the characteristics of the subducted oceanic crust (e.g. fractures affecting the extent of partial melting of the mantle wedge; Miller *et al.*, 1992), or to changes in structural features of the overriding plate affecting its response to subduction-induced stress (e.g. Singer & Myers, 1992).

Implications for continental crust formation processes

Enriched high-MgO andesites (e.g. Kelemen *et al.*, 2003) and intrusive equivalents of Archean age (sanukitoids) have geochemical features remarkably similar to those of the average continental crust. Therefore, studying their petrogenesis helps to understand the processes responsible for the formation of the continental crust. In a subduction-related context the genesis of this type of rocks is usually explained by either partial melting of mantle peridotite metasomatized by slab melts (e.g. Shirey & Hanson, 1984; Martin *et al.*, 2005; Tatsumi, 2006) or incomplete reaction of slab melts with mantle peridotite (Kelemen *et al.*, 2003; Rapp *et al.*, 2010). In both cases incompatible element enrichment is attributed to slab melt interaction with mantle peridotite.

Enriched Pilavo basaltic andesites are geochemically similar to Archean sanukitoids and, to a lesser extent, to Setouchi sanukites, except for the variably lower MgO and significantly lower Ni and Cr contents resulting from high-pressure fractionation of spinel-bearing olivine-clinopyroxenite. The processes of incompatible element enrichment occurring at Pilavo may therefore be of relevance for the debate on continental crust formation. Having shown that incompatible element enrichment of Pilavo basaltic andesites has resulted from intra-crustal RAFC processes within a juvenile mafic crust, we suggest that, although ultimately sourced in the slab component, incompatible elements in isotopically primitive andesites can be enriched not only via slab melt–mantle wedge interactions, but also at mid-crustal levels through refining processes within a juvenile mafic crust. The main requirement for this to occur, as suggested by the high r value of our modeling, is probably a sufficient thermal maturation of the lower to mid-crust achieved by a focused and sustained transit of magmas through the same crustal volume. The transit of arc magmas through the juvenile oceanic plateau crust accreted to the continent in the Late Cretaceous seems thus a viable process for the formation of isotopically primitive but geochemically enriched, continental crust-type rocks in the Western Cordillera of Ecuador (see also Chiaradia, 2009).

ACKNOWLEDGEMENTS

Thoughtful reviews by Andy Saunders and two anonymous reviewers helped to improve the quality of this work. Editorial handling by John Gamble and Marjorie Wilson is greatly appreciated. We thank A. Ulianov for precious technical support during LA-ICP-MS analyses, C.

Ginibre, K. Kouzmanov and J. Allibon for help with the microprobe analyses, and F. Capponi for whole-rock XRF analyses.

FUNDING

This study was funded by the Swiss National Science Foundation (projects N. 200021-109636 and 200020-117616).

SUPPLEMENTARY DATA

Supplementary data for this paper are available at *Journal of Petrology* online.

REFERENCES

Aguilera, E. (1998). The Chalupas and Chachimbiro geothermal fields in Ecuador. *Geothermal Resources Council Transactions* **22**, 247–251.

Amórtegui, A., Lapierre, H., Jaillard, E., Martelat, J.-E., Bosch, D., Bussy, F., Demant, A. & Brunet, P. (2005). Accreted oceanic fragments below the Western Cordillera of Ecuador. *6th International Symposium on Andean Geodynamics (ISAG 2005, Barcelona), Extended Abstracts* 42–45.

Annen, C., Blundy, J. D. & Sparks, R. S. J. (2006). The genesis of calc-alkaline intermediate and silicic magmas in deep crustal hot zones. *Journal of Petrology* **47**, 505–539.

Bacon, C. R. & Hirschmann, M. M. (1988). Mg/Mn partitioning as a test for equilibrium between coexisting Fe–Ti oxides. *American Mineralogist* **73**, 57–61.

Barazangi, M. & Isacks, B. (1976). Spatial distribution of earthquakes and subduction of the Nazca plate beneath South America. *Geology* **4**, 686–692.

Barragan, R., Geist, D., Hall, M., Larsen, P. & Kurz, M. (1998). Subduction controls on the compositions of lavas from the Ecuadorian Andes. *Earth and Planetary Science Letters* **154**, 153–166.

BGS & CODIGEM. (1999). *Mapa geologico de la Cordillera Occidental del Ecuador entre 0°–1° N*. Quito: Mision Britanica, CODIGEM.

Blundy, J. D. & Wood, B. J. (1991). Crystal-chemical controls on the partitioning of Sr and Ba between plagioclase feldspar, silicate melts, and hydrothermal solutions. *Geochimica et Cosmochimica Acta* **55**, 193–209.

Bohrson, W. A. & Spera, F. J. (2003). Energy-constrained open-system magmatic processes IV: Geochemical, thermal and mass consequences of energy-constrained recharge, assimilation and fractional crystallization (EC-RAFC). *Geochemistry, Geophysics, Geosystems* **4(2)**, 8002, doi:10.1029/2002GC000316.

Bourdon, E., Eissen, J. P., Gutscher, M. A., Monzier, M., Hall, M. L. & Cotten, J. (2003). Magmatic response to early aseismic ridge subduction: the Ecuadorian margin case (South America). *Earth and Planetary Science Letters* **205**, 123–138.

Brophy, J. G., Whittington, C. S. & Park, Y.-R. (1999). Sector-zoned augite megacrysts in Aleutian high alumina basalts: implications for the conditions of basalt crystallization and the generation of calc-alkaline series magmas. *Contributions to Mineralogy and Petrology* **135**, 277–290.

Browne, B. L. & Gardner, J. E. (2005). The influence of magma ascent path on the texture, mineralogy, and formation of hornblende reaction rims. *Earth and Planetary Science Letters* **246**, 161–176.

Bryant, J. A., Yogodzinski, G. M., Hall, M. L., Lewicki, J. L. & Bailey, D. G. (2006). Geochemical constraints on the origin of volcanic rocks from the Andean Northern Volcanic Zone, Ecuador. *Journal of Petrology* **47**, 1147–1175.

Chiaradia, M. (2009). Adakite-like magmas from fractional crystallization and melting–assimilation of mafic lower crust (Eocene Macuchi arc, Western Cordillera, Ecuador). *Chemical Geology* **265**, 468–487.

Chiaradia, M. & Fontboté, L. (2001). Radiogenic lead signatures in Au-rich VHMS ores and associated volcanic rocks of the Early Tertiary Macuchi island arc (Western Cordillera of Ecuador). *Economic Geology* **96**, 1361–1378.

Chiaradia, M., Müntener, O., Beate, B. & Fontignie, D. (2009). Adakite-like volcanism of Ecuador: lower crust magmatic evolution and recycling. *Contributions to Mineralogy and Petrology* **158**, 563–588.

Clynne, M. A., Muffler, L. J. P., Siems, D. F., Taggart, J. E., Jr & Bruggman, P. (2008). Major and EDXRF trace element chemical analyses of volcanic rocks from Lassen Volcanic National Park and vicinity, California. *US Geological Survey Open-File Report* **2008–1091**, 1–10.

Corredor, F. (2003). Seismic strain rates and distributed continental deformation in the northern Andes and three-dimensional seismotectonics of the northwestern South America. *Tectonophysics* **372**, 147–166.

Crawford, A. J., Falloon, T. J. & Eggins, S. (1987). The origin of island arc high-alumina basalts. *Contributions to Mineralogy and Petrology* **97**, 417–430.

Davidson, J., Turner, S., Handley, H., Macpherson, C. & Dosseto, A. (2007). Amphibole 'sponge' in arc crust? *Geology* **35**, 787–790.

Dickinson, W. R. (1975). Potash–depth (K–h) relations in continental margin and intra-oceanic magmatic arcs. *Geology* **3**, 53–56.

Dufek, J. & Bergantz, G. W. (2005). Lower crustal magma genesis and preservation: a stochastic framework for the evaluation of basalt–crust interaction. *Journal of Petrology* **46**, 2167–2195.

Ego, F., Sébrier, M., Lavenu, A., Yepes, H. & Egues, A. (1996). Quaternary state of stress in the Northern Andes and the restraining bend model for the Ecuadorian Andes. *Tectonophysics* **259**, 101–116.

Feig, S. T., Koepke, J. & Snow, J. E. (2006). Effect of water on tholeiitic basalt phase equilibria: an experimental study under oxidizing conditions. *Contributions to Mineralogy and Petrology* **152**, 611–638.

Feininger, T. (1987). Allochthonous terranes in the Andes of Ecuador and northwestern Peru. *Canadian Journal of Earth Sciences* **24**, 266–278.

Feininger, T. & Seguin, M. K. (1983). Bouguer gravity anomaly field and inferred crustal structure of continental Ecuador. *Geology* **11**, 40–44.

Finney, B., Turner, S., Hawkesworth, C., Larsen, J., Nye, C., Rhiannon, G., Bindeman, I. & Eichelberger, J. (2008). Magmatic differentiation at an island-arc caldera: Okmok Volcano, Aleutian Islands, Alaska. *Journal of Petrology* **49**, 857–884.

Foden, J. D. & Green, D. H. (1992). Possible role of amphibole in the origin of andesite: some experimental and natural evidence. *Contributions to Mineralogy and Petrology* **109**, 479–493.

Frost, B. R. & Lindsley, D. H. (1991). Occurrence of iron–titanium oxides in igneous rocks. In: Lindsley, D. H. (ed.) *Oxide Minerals. Mineralogical Society of America, Reviews in Mineralogy* **25**, 433–468.

Gill, J. B. (1981). *Orogenic Andesites and Plate Tectonics*. New York: Springer.

Graindorge, D., Calahorrano, A., Charvis, P., Collot, J. Y. & Bethoux, N. (2004). Deep structure of the Ecuador convergent margin and the Carnegie Ridge, possible consequences on great earthquakes recurrence interval. *Geophysical Research Letters* **31**, doi:10.1029/2003GL018803.

Grove, T. L., Elkins-Tanton, L. T., Parman, S. W., Chatterjee, N., Müntener, O. & Gaetani, G. A. (2003). Fractional crystallization and mantle-melting controls on calc-alkaline differentiation trends. *Contributions to Mineralogy and Petrology* **145**, 515–533.

Guillier, B., Chatelain, J. L., Jaillard, E., Yepes, H., Poupinet, G. & Fels, J. F. (2001). Seismological evidence on the geometry of the orogenic system in central–northern Ecuador (South America). *Geophysical Research Letters* **28**, 3749–3752.

Gutscher, M. A., Malavieille, J., Lallemand, S. & Collot, J. Y. (1999). Tectonic segmentation of the North Andean margin: impact of the Carnegie Ridge collision. *Earth and Planetary Science Letters* **168**, 255–270.

Harpp, K., Wanless, V. D., Otto, R. H., Hoernle, K. & Werner, R. (2005). The Cocos and Carnegie aseismic ridges: a trace element record of long-term plume–spreading center interaction. *Journal of Petrology* **46**, 109–133.

Hermann, J., Spandler, C., Hack, A. & Korsakov, A. V. (2006). Aqueous fluids and hydrous melts in high-pressure and ultra-high pressure rocks: Implications for element transfer in subduction zones. *Lithos* **92**, 399–417.

Hirose, K. (1997). Melting experiments of lherzolite KLB-1 under hydrous conditions and generation of high-magnesian andesitic melts. *Geology* **25**, 42–44.

Hora, J. M., Singer, B. S., Wörner, G., Beard, B. L., Jicha, B. R. & Johnson, C. M. (2009). Shallow and deep crustal control on differentiation of calc-alkaline and tholeiitic magma. *Earth and Planetary Science Letters* **285**, 75–86.

Jackson, S. (2008). LAMTRACE data reduction software for LA-ICP-MS. In: Sylvester, P. (ed.) Laser Ablation ICP-MS in the Earth Sciences: current practices and outstanding issues. Mineralogical Association of Canada Short Course. *Mineralogical Association of Canada Short Course Series* **40**, 305–307.

Jackson, S. E., Longerich, H. P., Dunning, G. R. & Fryer, B. J. (1992). The application of laser ablation microprobe–inductively coupled plasma–mass spectrometry (LAM–ICP–MS) to *in situ* trace element determinations in minerals. *Canadian Mineralogist* **30**, 1049–1064.

Jaillard, E., Soler, P., Carlier, G. & Mourier, T. (1990). Geodynamic evolution of the northern and central Andes during early-to-middle Mesozoic times: a Tethyan model. *Journal of the Geological Society, London* **147**, 1009–1022.

Jaillard, E., Benítez, S. & Mascle, G. H. (1997). Les déformations paléogenes de la zone d'avant-arc sud-équatorienne en relation avec l'évolution géodynamique. *Bulletin de la Société Géologique de France* **168**, 403–412.

Kägi, R. (2001). The liquid line of descent of hydrous, primary, calc-alkaline magmas under elevated pressure. An experimental approach, PhD thesis, ETH Zuürich, 115 pp.

Kelemen, P. B., Yogodzinski, G. M. & Scholl, D. M. (2003). Along-strike variation in the Aleutian Island Arc: Genesis of high Mg# andesite and implications for continental crust. In: Eiler, J. (ed.) *Inside the Subduction Factory. Geophysical Monograph, American Geophysical Union* **138**, 223–276.

Kelemen, P. B., Hanghoj, K. & Greene, A. R. (2004). One view of the geochemistry of subduction-related magmatic arcs, with an emphasis on primitive andesite and lower crust. In: Holland, H. D. & Turekian, K. K. (eds) *Treatise on Geochemistry*. Amsterdam: Elsevier, pp. pp, pp. 593–659.

Kerr, A. C., Aspden, J. A., Tarney, J. & Pilatasig, L. F. (2002). The nature and provenance of accreted oceanic blocks in western Ecuador: geochemical and tectonic constraints. *Journal of the Geological Society, London* **159**, 577–594.

Kessel, R., Schmidt, M. W., Ulmer, P. & Pettke, T. (2005). Trace element signature of subduction-zone fluids, melts and supercritical liquids at 120–180 km depth. *Nature* **437**, 724–727.

Kincaid, C. & Griffiths, R. W. (2004). Variability in flow and temperatures within mantle subduction zones. *Geochemistry, Geophysics, Geosystems* **5**, Q06002, doi:10.1029/2003GC000666.

Kushiro, I. (1969). The system forsterite–diopside–silica with and without water at high pressures. *American Journal of Science* **267A**, 269–294.

Leake, B. E., Woolley, A. R., Arps, C. E. S. *et al.* (1997). Nomenclature of amphiboles; report of the Subcommittee on Amphiboles of the International Mineralogical Association Commission on New Minerals and Mineral Names. *European Journal of Mineralogy* **9**, 623–651.

Le Bas, M. J., Le Maitre, R. W., Streckeisen, A. & Zanettin, B. (1986). A chemical classification of volcanic rocks based on the total alkali–silica diagram. *Journal of Petrology* **27**, 745–750.

Lee, C.-T. A., Cheng, X. & Horodyskyj, U. (2006). The development and refinement of continental arcs by primary basaltic magmatism, garnet pyroxenite accumulation, basaltic recharge and delamination: insights from the Sierra Nevada. *Contributions to Mineralogy and Petrology* **151**, 222–242.

Lepage, L. (2003). ILMAT: an Excel worksheet for ilmenite–magnetite geothermometry and geobarometry. *Computers and Geosciences* **29**, 673–678.

Lindsley, D. H. & Spencer, K. J. (1982). Fe–Ti oxide geothermometry: Reducing analyses of coexisting Ti-magnetite (Mt) and ilmenite (Ilm). Abstracts, AGU 1982 Spring Meeting. *EOS Transactions, American Geophysical Union* **63(18)**, 471.

Litherland, M., Aspden, J. A. & Jemielita, R. A. (1994). *The Metamorphic Belts of Ecuador*. Keyworth: British Geological Survey.

Longerich, H. P., Jackson, S. E. & Günther, D. (1996). Laser ablation–inductively coupled plasma–mass spectrometric transient signal data acquisition and analyte concentration calculation. *Journal of Analytical Atomic Spectrometry* **11**, 899–904.

Lonsdale, P. (1978). Ecuadorian subduction system. *AAPG Bulletin* **62(12)**, 2454–2477.

Mamberti, M., Lapierre, H., Bosch, D., Jaillard, E., Ethien, R., Hernandez, J. & Polvé, M. (2003). Accreted fragments of the Late Cretaceous Caribbean–Colombian Plateau in Ecuador. *Lithos* **66**, 173–199.

Martin, H., Smithies, R. H., Rapp, R., Moyen, J.-F. & Champion, D. (2005). An overview of adakite, tonalite–trondhjemite–granodiorite (TTG), and sanukitoid: relationships and some implications for crustal evolution. *Lithos* **79**, 1–24.

Mashima, H. (2004). Time scale of magma mixing between basalt and dacite estimated for the Saga–Futagoyama volcanic rocks in northwest Kyushu, southwest Japan. *Journal of Volcanology and Geothermal Research* **131**, 333–349.

Mason, D. R. (1978). Compositional variations in ferromagnesian minerals from porphyry copper-generating and barren intrusions of the Western Highlands, Papua New Guinea. *Economic Geology* **73**, 878–890.

Miller, D. M., Langmuir, C. H., Goldstein, S. L. & Franks, A. L. (1992). The importance of parental magma composition to calc-alkaline and tholeiitic evolution: evidence from Umnak Island in the Aleutians. *Journal of Geophysical Research* **97(B1)**, 321–343.

Miyashiro, A. (1974). Volcanic rock series in island arcs and active continental margins. *American Journal of Science* **274**, 321–355.

Müntener, O., Kelemen, P. B. & Grove, T. L. (2001). The role of H_2O during crystallization of primitive arc magmas under uppermost

mantle conditions and genesis of igneous pyroxenites: an experimental study. *Contributions to Mineralogy and Petrology* **141**, 643–658.

Panjasawatwong, Y., Danyushevsky, L. V., Crawford, A. J. & Harris, K. L. (1995). An experimental study of the effects of melt composition on plagioclase–melt equilibria at 5 and 10 kbar: implications for the origin of magmatic high-An plagioclase. *Contributions to Mineralogy and Petrology* **118**, 420–432.

Pennington, W. D. (1981). Subduction of the eastern Panama basin and seismotectonics of northwestern South America. *Journal of Geophysical Research* **86(B11)**, 10753–10770.

Petford, N. & Gallagher, K. (2001). Partial melting of mafic (amphibolitic) lower crust by periodic influx of basaltic magma. *Earth and Planetary Science Letters* **193**, 483–499.

Pin, C., Briot, D., Bassin, C. & Poitrasson, F. (1994). Concomitant separation of strontium and samarium–neodymium for isotopic analysis in silicate samples, based on specific extraction chromatography. *Analytica Chimica Acta* **298**, 209–217.

Plank, T. (2005). Constraints from thorium/lanthanum on sediment recycling at subduction zones and the evolution of the continents. *Journal of Petrology* **46**, 921–944.

Plank, T. & Langmuir, C. H. (1998). The chemical composition of subducting sediment and its consequences for the crust and mantle. *Chemical Geology* **145**, 325–394.

Plank, T., Cooper, L. B. & Manning, C. E. (2009). Emerging geothermometers for estimating slab surface temperatures. *Nature Geoscience* **2**, 611–615.

Prévot, R., Chatelain, J.-L., Guillier, B. & Yepes, H. (1996). Tomographie des Andes Equatoriennes: évidence d'une continuité des Andes Centrales. *Comptes Rendus de l'Académie des Sciences, Série II* **323**, 833–840.

Rapp, R. P., Shimizu, N., Norman, M. D. & Applegate, G. S. (1999). Reaction between slab-derived melts and peridotite in the mantle wedge: experimental constraints at 3·8 GPa. *Chemical Geology* **160**, 335–356.

Rapp, R. P., Norman, M. D., Laporte, D., Yaxley, G. M., Martin, H. & Foley, S. F. (2010). Continent formation in the Archean and chemical evolution of the cratonic lithosphere: melt–rock reaction experiments at 3–4 GPa and petrogenesis of Archean Mg-diorites (sanukitoids). *Journal of Petrology* **51**, 1237–1266.

Reubi, O. & Blundy, J. (2008). Assimilation of plutonic roots, formation of high-K 'exotic' melt inclusions and genesis of andesitic magmas at Volcán de Colima, Mexico. *Journal of Petrology* **49**, 2221–2243.

Richards, J. P. (2003). Tectono-magmatic precursors for porphyry Cu–(Mo–Au) deposit formation. *Economic Geology* **98**, 1515–1533.

Rudnick, R. L. & Gao, S. (2004). Composition of the continental crust. In: Holland, H. D. & Turekian, K. K. (eds) *Treatise on Geochemistry*. Amsterdam: Elsevier, pp. 1–64.

Rutherford, M. J. (2008). Magma ascent rates. In: Putirka, K. D. & Tepley, F. J., III (eds) *Minerals, Inclusions and Volcanic Processes. Mineralogical Society of America and Geochemical Society Reviews, in Mineralogy and Geochemistry* **69**, 241–271.

Rutherford, M. J. & Devine, J. D. (2003). Magmatic conditions and magma ascent as indicated by hornblende phase equilibria and reactions in the 1995–2002 Soufrière Hills magma. *Journal of Petrology* **44**, 1433–1454.

Rutherford, M. J. & Hill, P. M. (1993). Magma ascent rates from amphibole breakdown: An experimental study applied to the 1980–1986 Mount St Helens eruptions. *Journal of Geophysical Research* **98(B11)**, 19667–19685.

Sato, H. (1975). Diffusion coronas around quartz xenocrysts in andesite and basalt from Tertiary volcanic region in Northeastern Shikoku, Japan. *Contributions to Mineralogy and Petrology* **50**, 49–64.

Scaillet, B. & Evans, B. W. (1999). The 15 June 1991 Eruption of Mount Pinatubo. I. Phase equilibria and pre-eruption *P–T–fO2–f*H_2O conditions of the dacite magma. *Journal of Petrology* **40**, 381–411.

Shaw, H. R. (1974). Diffusion of H_2O in granitic liquids; Part 1, Experimental data; Part 2, Mass transfer in magma chambers. In: Hofmann, W., Giletti, B. J., Yoder Jr., H.S. & Yund, R.A. (eds) Geochemical Transport and Kinetics. Washington: Carnegie Institution of Washington, pp. 139–170.

Shimoda, G., Tatsumi, Y., Nohda, S., Ishizaka, K. & Jahn, B. M. (1998). Setouchi high-Mg andesites revisited: geochemical evidence for melting of subducting sediments. *Earth and Planetary Science Letters* **160**, 479–492.

Shirey, S. B. & Hanson, G. N. (1984). Mantle-derived Archaean monzodiorites and trachyandesites. *Nature* **310**, 222–224.

Singer, B. S. & Myers, J. D. (1990). Intra-arc extension and magmatic evolution in the central Aleutian arc, Alaska. *Geology* **18**, 1050–1053.

Singh, J. & Johannes, W. (1996). Dehydration melting of tonalites. 2. Composition of melts and solids. *Contributions to Mineralogy and Petrology* **125**, 26–44.

Sisson, T. W. & Grove, T. L. (1993). Experimental investigations of the role of H_2O in calc-alkaline differentiation and subduction zone magmatism. *Contributions to Mineralogy and Petrology* **113**, 143–166.

Sisson, T. W., Ratajeski, K., Hankins, W. B. & Glazner, A. F. (2005). Voluminous granitic magmas from common basaltic sources. *Contributions to Mineralogy and Petrology* **148**, 635–661.

Spikings, R. A., Winkler, W., Hughes, R. A. & Handler, R. (2005). Thermochronology of allochthonous terranes in Ecuador: Unravelling the accretionary and post-accretionary history of the Northern Andes. *Tectonophysics* **399**, 195–220.

Stimac, J. A. & Pearce, T. H. (1992). Textural evidence of mafic–felsic magma interaction in dacite lavas, Clear Lake. *American Mineralogist* **77**, 795–809.

Storkey, A. C., Hermann, J., Hand, M. & Buick, I. S. (2005). Using *in situ* trace-element determinations to monitor partial-melting processes in metabasites. *Journal of Petrology* **46**, 1283–1308.

Sun, S. S. & McDonough, W. F. (1989). Chemical and isotopic systematics of oceanic basalts: implications for mantle composition and processes. In: Saunders, A. D. & Norry, M. J. (eds) *Magmatism in the Ocean Basins. Geological Society, London, Special Publications* **42**, 313–346.

Tanaka, T., Togashi, S., Kamioka, H., Amakawa, H., Kagami, H., Hamamoto, T., Yuhara, M., Orihashi, Y., Yoneda, S., Shimizu, H., Kunimaru, T., Takahashi, K., Yanagi, Y., Nakano, T., Fujimaki, H., Shinjo, R., Asahara, Y., Tanimizu, M. & Dragusanu, C. (2000). JNdi-1: a neodymium isotopic reference in consistency with La Jolla neodymium. *Chemical Geology* **168**, 279–281.

Tatsumi, Y. (1989). Migration of fluid phases and genesis of basalt magmas in subduction zones. *Journal of Geophysical Research* **94(B4)**, 4697–4707.

Tatsumi, Y. (2006). High-Mg andesites in the Setouchi volcanic belt, southwestern Japan: analogy to Archean magmatism and continental crust formation? *Annual Review of Earth and Planetary Sciences* **34**, 467–499.

Tatsumi, Y. & Kogiso, T. (2003). The subduction factory: its role in the evolution of the Earth's crust and mantle. In: Larter, R. D. & Leat, P. T. (eds) *Intra-oceanic Subduction Systems. Geological Society, London, Special Publications* **219**, 55–80.

Tatsumi, Y., Shukuno, H., Sato, K., Shibata, T. & Yoshikawa, M. (2003). The petrology and geochemistry of high-magnesium andesites at the western tip of the Setouchi Volcanic Belt, SW Japan. *Journal of Petrology* **44**, 1561–1578.

Taylor, S. R., Capp, A. C., Graham, A. L. & Blake, D. H. (1969). Trace element abundances in andesites. *Contributions to Mineralogy and Petrology* **23**, 1–26.

Thornber, C. R., Pallister, J. S., Lowers, H. A., Rowe, M. C., Mandeville, C. W. & Meeker, G. P. (2008). Chemistry, mineralogy, and petrology of amphibole in Mount St. Helens 2004–2006 dacite. In: Sherrod, D. R., Scott, W. E. & Stauffer, P. H. (eds) *A Volcano Rekindled; the Renewed Eruption of Mount St. Helens, 2004–2006. US Geological Survey Professional Papers* **1750**, 727–753.

Todt, W., Cliff, R. A., Hanser, A. & Hofmann, A. W. (1996). Evaluation of a ^{202}Pb–^{205}Pb double spike for high-precision lead isotope analysis. In: Basu, A. & Hart, S. (eds) *Earth Processes: Reading the Isotopic Code. Geophysical Monograph, American Geophysical Union* **95**, 429–437.

Vallejo, C., Spikings, R. A., Luzieux, L., Winkler, W., Chew, D. & Page, L. (2006). The early interaction between the Caribbean Plateau and the NW South American Plate. *Terra Nova* **18**, 264–269.

Vallejo, C., Winkler, W., Spikings, R. A., Luzieux, L., Heller, F. & Bussy, F. (2009). Mode and timing of terrane accretion in the forearc of the Andes in Ecuador. *In: Geological Society of America, Memoirs* **204**, 197–216.

van Keken, P. E., Kiefer, B. & Peacock, S. M. (2002). High-resolution models of subduction zones: implications for mineral dehydration reactions and the transport of water into the deep mantle. In: Kay, S.M., Ramos, V.A. & Dickinson, W.R. (eds) Backbone of the Americas: Shallow Subduction, Plateau Uplift, and Ridge and Terrane Collision. *Geological Society of America Memoir* **204**, 197–216.

White, W. M., McBirney, A. R. & Duncan, R. A. (1993). Petrology and geochemistry of the Galapagos Islands: portrait of a pathological mantle plume. *Journal of Geophysical Research* **98**, 19533–19563.

Wood, B. J. & Turner, S. P. (2009). Origin of primitive high-Mg andesite: Constraints from natural examples and experiments. *Earth and Planetary Science Letters* **283**, 59–66.

Yogodzinski, G. M., Volynets, M. P., Koloskov, A. V., Seliverstov, N. I. & Matvenkov, V. V. (1994). Magnesian andesites and the subduction component in a strongly calc-alkaline series at Piip volcano, far western Aleutians. *Journal of Petrology* **35**, 163–204.

Zindler, A. & Hart, S. (1986). Chemical geodynamics. *Annual Review of Earth and Planetary Sciences* **14**, 493–571.